Applied Mathematics and Computation 384 (2020) 125383

Contents lists available at ScienceDirect

Applied Mathematics and Computation

journal homepage: www.elsevier.com/locate/amc

A two-dimensional multi-species model for different *Listeria monocytogenes* biofilm structures and its numerical simulation☆

Eva Balsa-Canto[a], Alejandro López-Núñez[b], Carlos Vázquez[b,*]

[a] *Process Engineering Group, IIM-CSIC. Spanish Council for Scientific Research. Eduardo Cabello 6, Vigo 36208, Spain*
[b] *Department of Mathematics and CITIC, University of A Coruña, Campus Elviña s/n, 15071–A Coruña, Spain*

ARTICLE INFO

Article history:
Received 30 September 2019
Revised 15 April 2020
Accepted 17 May 2020

Keywords:
Biofilms
Continuum models
Nonlinear systems of PDEs
Finite differences
Level set methods

ABSTRACT

In this work we propose a two-dimensional multi-species model to describe the dynamics of biofilms formed by the pathogenic bacteria *Listeria monocytogenes*. Different *Listeria monocytogenes* strains produce biofilms with different structures, namely flat, honeycomb and clustered. Previous works showed that glucose impaired uptake and the appearance of damaged or dead cells are critical mechanisms underlying *Listeria monocytogenes* biofilm dynamics. Here we explicitly propose an extension of the two-dimensional multi-species model proposed by Alpkist and Klapper to account for those mechanisms. The result is a continuous two-dimensional multi-species model with non-linear detachment and mass action nutrient consumption. Moreover, we also propose a set of efficient numerical methods to solve the coupled model and we have developed their computer implementation from scratch in C/C++. Mainly based on finite differences schemes, these numerical techniques include Crank-Nicolson schemes for time discretization, Gibou's ghost node techniques and level set methods to cope with the free boundary associated to the determination of the time-dependent biofilm domain. To finish with, we compare our simulation results with the dynamics of real biofilms as observed in the laboratory. More precisely, by using model parameters calibrated to experiments, the numerical results clearly illustrate the performance of the proposed model and the numerical methods to reproduce the real dynamics of flat, clustered and honeycomb structures shown by different *Listeria monocytogenes* strains.

☆ ALN and CV acknowledge the funding by MINECO from Spanish Government (Grant MTM2016-76497-R) and by Xunta de Galicia (Grants GRC2014/044 and ED431C2018/033). ALN acknowledges FPU fellowship (FPU13/02191) from the Spanish Government program MECD-FPU. CV and ALN as members of CITIC also akcnowledge the grant ED431G 2019/01, funded by Consellería de Educación, Universidade e Formación Profesional of Xunta de Galicia through FEDER funds with 80%, from FEDER Galicia 2014-2020 Program and 20% from Secretaría Xeral de Universidades. EBC acknowledges funding from Contrato Programa and grant Ref. IN607B 2017/02 from Xunta de Galicia. All grants include FEDER funds.

* Corresponding author.
E-mail addresses: ebalsa@iim.csic.es (E. Balsa-Canto), alejandro.lopezn@udc.es (A. López-Núñez), carlosv@udc.es (C. Vázquez).

https://doi.org/10.1016/j.amc.2020.125383

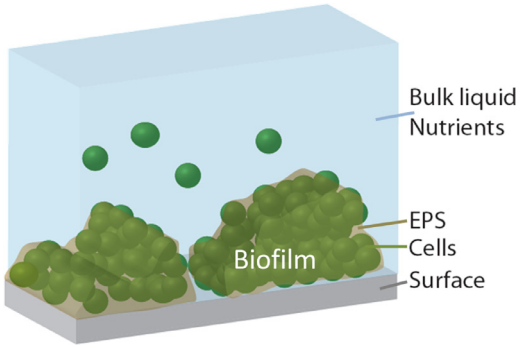

Fig. 1. Fundamental parts of a bacterial biofilm system

1. Introduction

The vast majority of bacteria tend to grow forming biofilm systems. A bacterial biofilm is a layer of cells anchored to a substrate layer that keeps them fed and embedded in the exopolisaccharides matrix (EPS), which is formed by polymers and grants protection to stress and removal, including biocides. Biofilm structures prevent bacteria from being washed out, in contrast to planktonic bacteria, and grant a safe environment where they can grow (provided that enough nutrients are available), and form different biological niches for those bacteria that are not able to compete in a fully homogeneus system.

The fundamental parts of a biofilm system (Fig. 1), are the surface (where bacteria are attached to), the proper biofilm (formed by one or more cell species and the EPS), the media (with nutrients), and the environmental conditions that determine the biofilm development (temperature, pH and hydrodynamics, among others).

There are beneficial biofilms [48], such as the ones used in water treatment plants (RBC, biological reactors), or the ones colonising rocks in rivers and lakes that help decontaminating waters, and harmful biofilms, such as the ones appearing in medical implants [52] or in the dental plaque [25].

Under the last category lie the biofilms formed by *Listeria monocytogenes*, a Gram-positive, food-borne pathogen specially problematic in food industry, that can cause systemic infections in immune compromised, pregnant or elderly patients [11]. Out of the around fifteen serotypes reported, there are three that account for the majority of human diseases: 1/2a, 1/2b and 4b [43]. Transmission of this pathogen to humans is primarily due to consumption of contaminated food, usually by contact with unhygienic work surfaces or facilities, where biofilms are found [21,43,49]. *L. monocytogenes* biofilms can emerge on common food contact surfaces, such as plastic, polypropylene, rubber, stainless steel or glass [41], and are protected from a variety of environmental factors, such as temperature, salt, sugar or pH [28]. They also tolerate better biocides, thus hindering the surface decontamination process to the point that many *L. monocytogenes* strains have been isolated from food processing plants despite the programs to sanitize them [10,38]. Miettinen et al. [27] showed that *L. monocytogenes* biofilms can persist several years in food processing plants. The most recent outbreaks in Spain and UK (2019) resulted in various death people and dozends of hospitalisations. Therefore it is of critical importance to unravel how L. monocytogenes form biofilms, their structure and their life cycle. These facts reflect the relevance of biofilms for the food industry [28] and identify *L. monocytogenes* as a major concern.

L. monocytogenes biofilms can depict different structures: mono-layer of adhered cells, flat unstructured multi-layers, honeycomb structures or clusters [6,7,14,26,35,37]. In order to study the dynamics of *L. monocytogenes* biofilms, there are two different approaches: experimental techniques and mathematical modelling. These approaches are not mutually exclusive and, in fact, produce better results when coupled together. The former includes many different techniques such as plaque count, widely used to analyse biofilms although unable to provide information about the structure [13], or microscopy based techniques, the most successful among them being confocal laser scanner microscopy (CLSM), that enables *in situ* and *in vivo* three-dimensional biofilm optical imaging [42]. In this context, recent works suggest several alternative work-flows and software tools for the systematic analysis of microscopy images, such as IMARIS (a commercial software that enables the reconstruction of 3-D structures); COMSTAT [18], ISA 3D [5], or PHLIP [31] (that allow quantifying CLSM images); BIOFILMDIVER [29] permits the quantification of biofilms areal porosity, covered area, diffusion distances or the spatio-temporal population distribution from 2-D images taken with epifluorescence and CLSM; or machine learning algorithms (that permits the analysis of scanning electron microscopy images [45]).

On the other hand, mathematical modelling is a tool that can complement the experimental studies due to its great capability of adaptation and change (easily including new mechanisms coming into play), and its reproducibility. Since the inception of the first simple empirical models around mid 20th century, mathematical models became much more complex, taking into account multiple species, both of bacteria and nutrients, together with different microbiological, chemical and physical processes giving place to multi-dimensional PDE systems. The evolution of biofilm mathematical models is linked to the evolution of the experimental analysis of biofilms [46].

This work pretends to take advantage of both tools: from the experimental one we take certain parameters obtained when calibrating the models to fit experimental measurements and from the mathematical modelling we adapt existing models and develop efficient numerical techniques to simulate them. Thus, we address the numerical solution of a continuous two-dimensional multi-species biofilm model describing biofilm formation in a hydrostatic setup. The model consists of a set of non-linear equations, that represent the dynamics of the biofilm system by considering the evolution of the steady-state Poisson equations related to the concentration of nutrients and the growth expansion pressure, and the time-dependent advection equations related to the active biomass and inactive biomass concentrations.

More precisely, starting from the model proposed by Alpkvist and Klapper [1], we introduce original modifications following the insights obtained by Balsa-Canto et al. [4] to incorporate several realistic structures and mechanisms. In particular, we modify nutrient consumption from Monod to mass action and we introduce a non-linear detachment due to biofilm aging, i.e. due to the presence of damaged or dead cells. The resulting innovative model is solved sequentially by using a set of highly efficient numerical methods such as the Crank-Nicolson method, Gibou's ghost nodes strategy [16] and level set methods first introduced in [33]. All these numerical methods have been implemented from scratch in C/C++. The involved model parameters were derived from [4], which contains a rigorous analysis of several one-dimensional (1-D) models that reproduce the dynamics of the *L. monocytogenes* L1A1 strain.

The here proposed model achieves the qualitative structure and temporal dynamics that describes the *Listeria monocytogenes* L1A1 strain which tends to form rough or flat structures. Previous work [4] showed that biofilm maximum height was quite sensitive to the growth rate and the rate of activation of detachment or inactivation rate. By modifying these parameters, the current model is also able to describe various typical structures developed by other strains of *L. monocytogenes*, such as clustered or honeycomb structures, and gives rise to biofilms of different heights. All in all, we end up obtaining a model that reproduces the experimental behaviour of several *L. monocytogenes* strains.

The structure of the paper reads as follows. In Section 2 the mathematical model is presented. Section 3 describes the numerical methods used, as well as the numerical strategy followed in order to solve numerically the presented model. Section 4 provides various numerical examples that illustrate the numerical solution obtained by the model. Finally, Section 5 serves as a summary of the results concluded by this work.

2. Mathematical model

In the recent work [4] the study of the dynamics of *L. monocytogenes* L1A1 strain is addressed by means of a 1-D model. This simplification could be achieved because L1A1 strain develops rather flat structures. For these flat structures, 1-D models and suitable numerical methods to simulate them can be considered (see [3,4], for example). The model was reconciled with experimental data through experimental data fitting and it was able to predict the dynamics of the biofilm height and nutrients consumption. The sensitivity analysis of the model revealed that nutrient impaired uptake and the presence of damaged or dead cells was critical to explain the system dynamics. It must be emphasized that in [4] the presence of damaged or dead cells was not modeled, but experimental data were used as an input to the system of partial differential equations.

However, the presence of internal channels, inner voids or other biofilm structures (such as rugose, mushroom-shaped or clustered biofilms), cannot be explained with 1-D models. Thus, in order to explore those different structures we need to define suitable two-dimensional (2-D) models that, in addition, should incorporate several components and/or species such as viable cells (from one or several microbial species), damaged or dead cells, EPS, various nutrients, etc. From now on, these models will be regarded as multi-species.

The first relevant multi-species model was presented in Wanner and Gujer [47], usually referred as W-G model. The model consists of a set of 1-D partial differential equations that describes the dynamics of a multi-microbial biofilm, usually with predefined microbial distributions. After that, more elaborated 2-D models were developed. Several authors suggested individual based models (see for instance, [22,23,34,44,50,51]) or cellular automaton based models (see [19,32], for example) to explain single and two-species biofilms.

The work by Wanner and Gujer [47] and the subsequent extension to the multidimensional case proposed by Alpkvist and Klapper [1] have been extensively used and thus the model we propose here is an extension with novel mechanisms of an already popular model. In particular, we adapt the model to account for two additional mechanisms that have been shown to be relevant for the dynamics of *L. monocytogenes* biofilms in batch cultures: glucose impaired uptake and biofilm aging [4].

This extension to the original Alpkist-Klapper model will enable us not only to recover flat but also clustered or honeycomb structures.

Alpkvist et al. [1] proposed a continuum model of the W-G type that allows the inclusion of multi-species as well as the study of spatial heterogeneities. When applying the model to a flat biofilm, it works as a W-G 1-D model, although it can also be used to capture different spatial structures. This model takes into account the active and inactive biomass of the same species and only one limiting nutrient. While referring to *active biomass* (represented by its volumetric fraction, v_1), we are considering the components of the biofilm actively reacting with the *nutrients*, the concentration of which is denoted by s. The *inactive biomass* (also represented by its volumetric fraction, v_2), includes all other materials that do not explicitly affect the nutrients concentration, such as damaged cells, dead cells or EPS.

The two dimensional domain of the problem, $\Omega = [0, L] \times [0, H]$, is represented in Fig. 2.

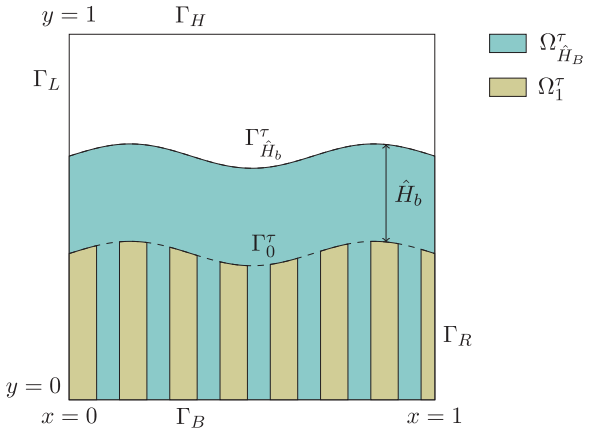

Fig. 2. Dimensionless solving domain for the 2D case.

At each time t, the domain is decomposed into two disjoint subdomains: the biomass region, Ω_1^t, and the bulk (the region without biomass), Ω_2^t. It must be noted that the regions Ω_1^t and Ω_2^t change with the evolution of the biomasses with time. Let us denote by Γ_0^t the free boundary separating Ω_1^t and Ω_2^t. In order to track the evolution of Γ_0^t, we introduce a time dependent *level set function,* ϕ, so that, at every time $t \geq 0$,

$$\Gamma_0^t = \{(x, y) \in \Omega / \phi(x, y, t) = 0\}.$$

In other words, Γ_0^t represents the level set zero of the function ϕ. Furthermore, the domains Ω_1^t and Ω_2^t can be represented in terms of the function ϕ as

$$\Omega_1^t = \{(x, y) \in \Omega / \phi(x, y, t) < 0\}, \quad \Omega_2^t = \{(x, y) \in \Omega / \phi(x, y, t) \geq 0\}.$$

Similarly, at a fixed given distance, H_b, from Γ_0^t we define the boundary

$$\Gamma_{H_b}^t = \{(x, y) \in \Omega / \phi(x, y, t) = H_b\},$$

which is the level set H_b of the function ϕ. This is a non-physical frontier above which there is enough availability of nutrients. The set $\Gamma_{H_b}^t$ also represents the upper boundary of the following domain

$$\Omega_{H_b}^t = \{(x, y) \in \Omega \ / \ \phi(x, y, t) < H_b\}.$$

Finally, the left and right boundaries of the domain Ω are denoted by

$$\Gamma_L = \{(x, y) \in \Omega \ / x = 0\}, \quad \Gamma_R = \{(x, y) \in \Omega \ / x = L\},$$

whereas the top and bottom boundaries are denoted by

$$\Gamma_B = \{(x, y) \in \Omega \ / y = 0\}, \quad \Gamma_H = \{(x, y) \in \Omega \ / y = H\}.$$

This model takes into account the following assumptions [1,2]:

i. The biofilm is described as a viscous fluid.
ii. Nutrients and biomasses concentrations are governed by a mass conservation equation.
iii. Active and inactive biomasses are of the same microbial species, thus implying that their density, ρ, is the same. Also, they are assumed to be incompressible, so that the density is constant.
iv. The biofilm system hosts reaction processes (production or consumption of nutrients or biomasses), transport processes (movement inside the same domain) or transference processes (movement between different domains).
v. Expansion or contraction of the biofilm is due to processes included in the model.
vi. The processes associated to the biomasses are much slower that the ones contributing to the nutrients evolution.
vii. Nutrients production or consumption is due to biotic or abiotic reaction processes.
viii. Nutrients are diluted in the media and, therefore, are present in the whole system, whereas biomass is not diluted and exists only inside the biofilm.

The description of the biofilm postulated by *(i)* allows to describe in a simple way the different interactions between species. Due to *(vi)*, nutrients are considered in a *quasi-steady* state.

Postulate *(viii)* implies that nutrients transport is governed by a diffusion mechanism, described by Fick's Law. On the other hand, biomasses transport is regulated by and advection process. The reaction included in biomasses equations cause an increase or decrease of the biomasses concentration which, in turn, translates into an increase or decrease of the volume

of the biofilm. The evolution of the biomasses concentration gives rise to a *growth expansion pressure, p*. The advective transport of biomass is understood as a movement away from the regions with high growth expansion pressure and is described through an advective *expansive velocity field*, $\vec{u}$, which depends on the pressure as stated in Darcy's Law. As previously indicated, the evolution of Γ_0^t depends on the evolution of the biomasses concentration. More precisely, all level sets of ϕ are going to move following the *normal velocity*, f_e, which represents an extension to all Ω of the normal component of $\vec{u}$, at Γ_0^t. In other words, f_e is the extension to Ω of $(\vec{u}\cdot\vec{n})_{|_{\Gamma_0^t}}$, where $\vec{n}$ is the vector normal to Γ_0^t.

The previous assumptions are completed with the following considerations [4]:

ix. Nutrients uptake (and, therefore, biomass growth), follows a mass action law.
x. Biofilm dynamics are affected by ageing.

Thus, the spatio-temporal variables of the model are

- $t \geq 0$: time,
- $(x, y) \in \Omega$: spatial coordinate,
- $v_i(x, y, t)$: active $(i = 1)$ and inactive $(i = 2)$ biomasses volumetric fractions,
- $s(x, y, t)$: nutrients concentration,
- $p(x, y, t)$: growth expansion pressure.
- $\vec{u}(x, y, t)$: expansive growth velocity field,
- $f_e(x, y, t)$: extended normal expansive velocity to Ω for the level set method,
- $\phi(x, y, t)$: level set function.

The model is given by the following set of equations [1]:

$$-D\nabla^2 s = R(v_1, v_2, s) \quad \text{in } \Omega_{H_b}^t, \tag{1}$$

$$-\rho\lambda\nabla^2 p = G_1(v_1, v_2, s) + G_2(v_1, v_2, s) \quad \text{in } \Omega_1^t, \tag{2}$$

$$\vec{u} = -\lambda\nabla p \quad \text{in } \Omega_1^t, \tag{3}$$

$$\partial_t\phi + f_e||\nabla\phi|| = 0 \quad \text{in } \Omega, \tag{4}$$

$$\rho(\partial_t v_i + \nabla\cdot(\vec{u}v_i)) = G_i(v_1, v_2, s), \text{ for } i = 1, 2, \quad \text{in } \Omega_1^t, \tag{5}$$

where D is the diffusion coefficient, $R(v_1, v_2, s)$ is the nutrients uptake rate and $G_i(v_1, v_2, s)$ are the biomasses growth rates ($i = 1$ for the active biomass and $i = 2$ for the inactive biomass). The second order elliptic partial differential Eq. (2) states that: when the biomass concentration increases, the pressure generated causes an expansion on the biofilm volume, whereas, when the biomass concentration decreases, the biofilm shrinks. The parameter λ is called the Darcy's parameter and depends on the viscosity of the media [15]. It can be proven [1] that p is proportional to λ^{-1}, so that we can take $\lambda = 1$.

From Eqs. (2) and (3) we get

$$-\lambda\nabla^2 p = -\nabla\cdot\vec{u} = \sum_{i=1}^{2}\frac{G_i(v_1, v_2, s)}{\rho}. \tag{6}$$

Next, by considering that $\nabla\cdot(\vec{u}v_i) = \vec{u}\cdot\nabla v_i + v_i\nabla\cdot\vec{u}$ and taking $\lambda = 1$, Eq. (5) becomes

$$\partial_t v_i - \nabla p\cdot\nabla v_i = \frac{G_i(v_1, v_2, s)}{\rho} - v_j\sum_{j=1}^{2}\frac{G_j(v_1, v_2, s)}{\rho}, \text{ for } i = 1, 2. \tag{7}$$

At this point, we would like to emphasize the proposed modification with respect to Alpkvist model [1]. First, we note that the third 1-D model proposed in [4] concludes that for L1A1 nutrients uptake is impaired and biofilm dynamics is affected by ageing, i.e. by the presence of inactive biomass. Therefore, we introduce the same mechanisms in the here proposed 2-D model. Thus, assuming that in our experimental scheme nutrients are not limited, we propose to modify the Monod term and use a linear nutrients uptake formulation. In addition, we replace the linear detachment by the inactive cell dependent detachment. Also note that the current model accounts for inactive cells, so that both equations are also coupled by the detachment term. Therefore, the proposed new reaction term can be expressed as

$$R(v_1, v_2, s) = \frac{-\rho v_1\mu s}{\mathcal{Y}}, \tag{8}$$

for the nutrients uptake, where

- $\mathcal{Y}$: growth yield,

- μ: maximum growth rate.

and

$$G_1(v_1, v_2, s) = v_1 \mu s - v_1 \frac{t_D^{-1}}{1 + \exp(K_d(D_{min} - mean(v_2)))} - v_1 k_i, \tag{9}$$

$$G_2(v_1, v_2, s) = v_1 k_i, \tag{10}$$

for the biomasses growth, where

- t_D: number of seconds per day,
- k_i: inactivation rate,
- K_d: rate of detachment activation,
- D_{min}: percentage of damaged or dead cells before detachment,
- $mean(v_2)$: mean concentration of inactive biomass.

Remark that, in this way, the detachment process starts when there is a given mean inert biomass in the biofilm and cells detach in all areas of the biofilm.

Finally, boundary conditions must be imposed. First of all, at the left and right boundaries, Γ_L and Γ_R respectively, we will consider periodic boundary conditions, i.e,

$$f(0, \cdot) = f(L, \cdot),$$

for any function f. Secondly, we consider the bottom boundary of the domain, Γ_B, impermeable, so that a no-flux condition is imposed, i.e,

$$\frac{\partial f}{\partial n} = 0 \text{ on } \Gamma_B.$$

In a similar manner, at the top boundary of the domain, Γ_H, a zero flux condition is imposed for the level set function. The value of H is taken large enough so that the boundary $\Gamma^t_{H_b}$ never leaves Ω. We assume that above $\Gamma^t_{H_b}$ there is enough nutrients availability. Furthermore, the concentration and flux of nutrients through $\Gamma^t_{H_b}$ must be continuous. Finally, active biomass, inactive biomass and pressure are set to be zero at Γ^t_0.

In summary, the model is described by Eqs. (1)–(4) and (7), with reaction terms (8)–(10), together with the following boundary conditions

$$s = s^* \text{ on } \Gamma^t_{H_b}, \quad \partial_y s = 0 \text{ on } \Gamma_B, \tag{11}$$

$$p = 0 \text{ on } \Gamma^t_0, \quad \partial_y p = 0 \text{ on } \Gamma_B, \tag{12}$$

$$\partial_y \phi = 0 \text{ on } \Gamma_H, \quad \partial_y \phi = 0 \text{ on } \Gamma_B, \tag{13}$$

$$v_1 = v_2 = 0 \text{ on } \Gamma^t_0, \quad \partial_y v_1 = \partial_y v_2 = 0 \text{ on } \Gamma_B, \tag{14}$$

where s^* is the maximum nutrients concentration, and periodic boundary conditions on Γ_L and Γ_R are considered.

2.1. Dimensionless model

For computational reasons, let us consider a dimensionless model by introducing the dimensionless spatial and temporal variables

$$X = \frac{x}{H}, \quad Y = \frac{y}{H}, \quad \tau = \frac{t}{t_D},$$

where t_D is the number of seconds per day and H is the height of the domain. The dimensionless nutrients, pressure, velocities, level set function and volumetric fractions are defined by

$$S = \frac{s}{s^*}, \quad P = \frac{\lambda t_D p}{H^2}, \quad \vec{U} = \vec{u}, \quad F_e = f_e, \quad \Phi = \phi, \quad V_i = v_i.$$

By applying the previous dimensionless spatio-temporal variables and unknowns, the system of Eqs. (1)–(4) and (7) becomes

$$-\nabla^2 S = -V_1 \hat{h}_T^2 S \text{ in } \Omega^\tau_{\hat{H}_b}, \tag{15}$$

$$-\nabla^2 P = V_1 \hat{\Psi} S - V_1 \mathcal{F}_D(V_2) \text{ in } \Omega^\tau_1, \tag{16}$$

Table 1
Parameters involved in the equations.

Parameter	Description
L, H	Domain length and height
H_b	Boundary layer height
ρ	Biomass Density
D	Diffusion coefficient
$\mathcal{Y}$	Growth yield
μ	Maximum growth rate
K_d	Rate of detachment activation
D_{min}	Percentage of damaged or dead cells
k_i	Inactivation rate
t_D	Number of seconds per day
s^*	Maximum nutrients concentration

$$\vec{U} = -\nabla P \text{ in } \Omega_1^\tau, \tag{17}$$

$$\partial_\tau \Phi + F_e ||\nabla \Phi|| = 0 \text{ in } \Omega, \tag{18}$$

$$\partial_\tau V_1 - \nabla P \cdot \nabla V_1 = V_1 \left[\hat{\Psi} S - (\mathcal{F}_{\mathcal{D}}(V_2) + \epsilon_2) - V_1 (\hat{\Psi} S - \mathcal{F}_{\mathcal{D}}(V_2)) \right] \text{ in } \Omega_1^\tau, \tag{19}$$

$$\partial_\tau V_2 - \nabla P \cdot \nabla V_2 = V_1 \epsilon_2 - V_2 \left(V_1 \hat{\Psi} S - V_1 \mathcal{F}_{\mathcal{D}}(V_2) \right) \text{ in } \Omega_1^\tau, \tag{20}$$

where

$$\mathcal{F}_{\mathcal{D}}(V_2) = \frac{1}{1 + \exp(K_d (D_{min} - mean(V_2)))}, \tag{21}$$

and the involved dimensionless constants are

$$\hat{h}_T^2 = \frac{H^2 \mu \rho}{\mathcal{Y} D}, \quad \hat{\Psi} = \mu s^* t_D, \quad \epsilon_2 = t_D k_i,$$

where the involved parameters are described in Table 1. The model is completed with the following dimensionless boundary conditions:

$$S = 1 \text{ on } \Gamma_{\hat{H}_b}^\tau, \quad \partial_Y S = 0 \text{ on } \Gamma_B, \tag{22}$$

$$P = 0 \text{ on } \Gamma_0^\tau, \quad \partial_Y P = 0 \text{ on } \Gamma_B, \tag{23}$$

$$\partial_Y \phi = 0 \text{ on } \Gamma_H, \quad \partial_Y \phi = 0 \text{ on } \Gamma_B, \tag{24}$$

$$V_1 = V_2 = 0 \text{ on } \Gamma_0^\tau, \quad \partial_Y V_1 = \partial_Y V_2 = 0 \text{ on } \Gamma_B, \tag{25}$$

jointly with periodic boundary conditions on Γ_L and Γ_R.

3. Numerical methods

In order to solve the system (15)–(20) jointly with the boundary conditions we consider a finite difference discretization in the time and spatial domain. As the equations involved in the system are coupled, we develop a sequential solution of them. Each equation needs specific numerical techniques. Therefore, in the following section we first introduce general notations associated to the finite differences discretization and briefly sketch the steps of the global algorithm. Next sections are devoted to the description of particular numerical techniques proposed for the equations to be solved at each step of the global algorithm. Note that we have chosen efficient numerical techniques which are suitable for the PDE problem at each step. Although we have obtained a good numerical convergence and stability behaviour, the theoretical analysis of the convergence of the global algorithm is an open problem which is out of the scope of the present article. The computer implementation of the proposed global algorithm has provided the numerical results shown in Section 4. These numerical results illustrate the agreement with the experiments in the laboratory, so that the proposed model has been validated.

All the codes corresponding to the numerical methods have been developed from scratch in C/C++, so that no commercial or professional software has been used.

3.1. General notations and global algorithm

In order to describe the numerical strategy, let us introduce certain general notations. First of all, as we are working in a finite differences framework, let M_X and M_Y be the number of spatial intervals in directions X and Y, respectively, and let N be the number of time intervals. For the sake of simplicity, let us consider a square domain with $H = L$ and let us take $M_X = M_Y = M$. Therefore, we can define the temporal and spatial steps of the finite different mesh as $\Delta\tau = T_{max}/N$ and $\Delta X = \Delta Y = 1/M$. Thus, the spatial nodes of the finite differences mesh are $(X_i, Y_j) = (i\Delta X, j\Delta Y)$, with $i, j = 0, \dots, M$ and the time nodes are $\tau_n = n\Delta\tau$, with $n = 0, \dots, N$. Moreover, the approximations of the unknowns of the system at the finite differences nodes are denoted by

- $S^n_{i,j} \approx S(X_i, Y_j, \tau_n)$, with $i, j = 0, \dots, M$ and $n = 0, \dots, N$,
- $P^n_{i,j} \approx P(X_i, Y_j, \tau_n)$, with $i, j = 0, \dots, M$ and $n = 0, \dots, N$,
- $\Phi^n_{i,j} \approx \Phi(X_i, Y_j, \tau_n)$, with $i, j = 0, \dots, M$ and $n = 0, \dots, N$,
- $V1^n_{i,j} \approx V_1(X_i, Y_j, \tau_n)$, with $i, j = 0, \dots, M$ and $n = 0, \dots, N$,
- $V2^n_{i,j} \approx V_2(X_i, Y_j, \tau_n)$, with $i, j = 0, \dots, M$ and $n = 0, \dots, N$.

As we are dealing with a time dependent biofilm domain, it will come in handy to introduce the indicator function $\aleph^n$, that identifies the nodes of the discretization that lie inside the biofilm domain at time τ_n, $\Omega_1^{\tau_n}$, and those that do not lie inside. This indicator function is defined in terms of the level set function as follows (note that the boundary of the biofilm domain corresponds to the zero level set):

$$\aleph^n(X, Y) = \begin{cases} 1, & \text{if } \Phi(X, Y, \tau^n) < 0, \\ 0, & \text{otherwise.} \end{cases} \tag{26}$$

Analogously, as the solving domain of the nutrients equation at time τ_n, $\Omega_{\hat{H}_b}^{\tau_n}$, includes part of the bulk (see Fig. 2), the indicator function $\aleph_S^n$ identifies the nodes of the discretization that lie inside $\Omega_{\hat{H}_b}^{\tau_n}$, and those that do not lie inside. This function is defined in terms of the level set function as

$$\aleph_S^n(X, Y) = \begin{cases} 1, & \text{if } \Phi(X, Y, \tau_n) < \hat{H}_b, \\ 0, & \text{otherwise.} \end{cases} \tag{27}$$

As with the rest of the involved functions, we use the notation $\aleph^n_{i,j} \approx \aleph^n(X_i, Y_j)$ and $\aleph^n_{S_{i,j}} \approx \aleph^n_S(X_i, Y_j)$, with $i, j = 0, \dots, M$ and $n = 0, \dots, N$.

Finally, as we are imposing periodic boundary conditions at Γ_L and Γ_R, we consider the identities

$$\mathcal{Q}^n_{M,j} = \mathcal{Q}^n_{0,j}, \quad \forall j = 0, \dots, M, \quad \forall n = 0, \dots, N,$$

where $\mathcal{Q}^n_{i,j} \approx \mathcal{Q}(X_i, Y_j, \tau_n)$ for any function or unknown, $\mathcal{Q}$, of the problem. In practise, this means that we are only considering the unknowns corresponding to the indices $i = 0, \dots, M-1$.

The model presented in Section 2 consist of a system of coupled differential equations. It is not possible to compute the analytical solution and solving the whole system at once requires a great effort from the numerical point of view. Therefore, the idea is to solve sequentially the involved equations at each time step. Thus, the global algorithm reads as follows (see Fig. 3):

1. Initialise the variables V_1^0, V_2^0 and Φ^0.
2. Start the temporal loop (indexed by n, corresponding to time τ^n).
3. Solve the nutrients Eq. (15).
4. Solve the pressure Eq. (16).
5. Compute the normal extended velocity, F_e, that moves the level sets by applying Eq. (17) and the velocity extension method.
6. Advance one time step in the level set Eq. (18).
7. With the new level set function, Φ^{n+1}, define the updated solving domains, $\Omega_1^{\tau_{n+1}}$ and $\Omega_{\hat{H}_b}^{\tau_{n+1}}$, the updated domain representing the bulk, $\Omega_2^{\tau_{n+1}}$ and the updated boundaries, $\Gamma_0^{\tau_{n+1}}$ and $\Gamma_{\hat{H}_b}^{\tau_{n+1}}$.
8. Advance one time step in the active biomass Eq. (19).
9. Advance one time step in the inactive biomass Eq. (20).
10. If $n + 1 < N$, repeat the process from step 3.

The applied numerical methods vary depending on which equation is being solved, due to the particularities of each one. In next sections we describe the different methods.

3.2. Numerical methods for the nutrients and pressure equations

The semi-linear Poisson equations governing the nutrients (15) and the expansive growth pressure (16), are solved at each time iteration. As the solving process is decoupled by solving the model sequentially, we must use the values of the

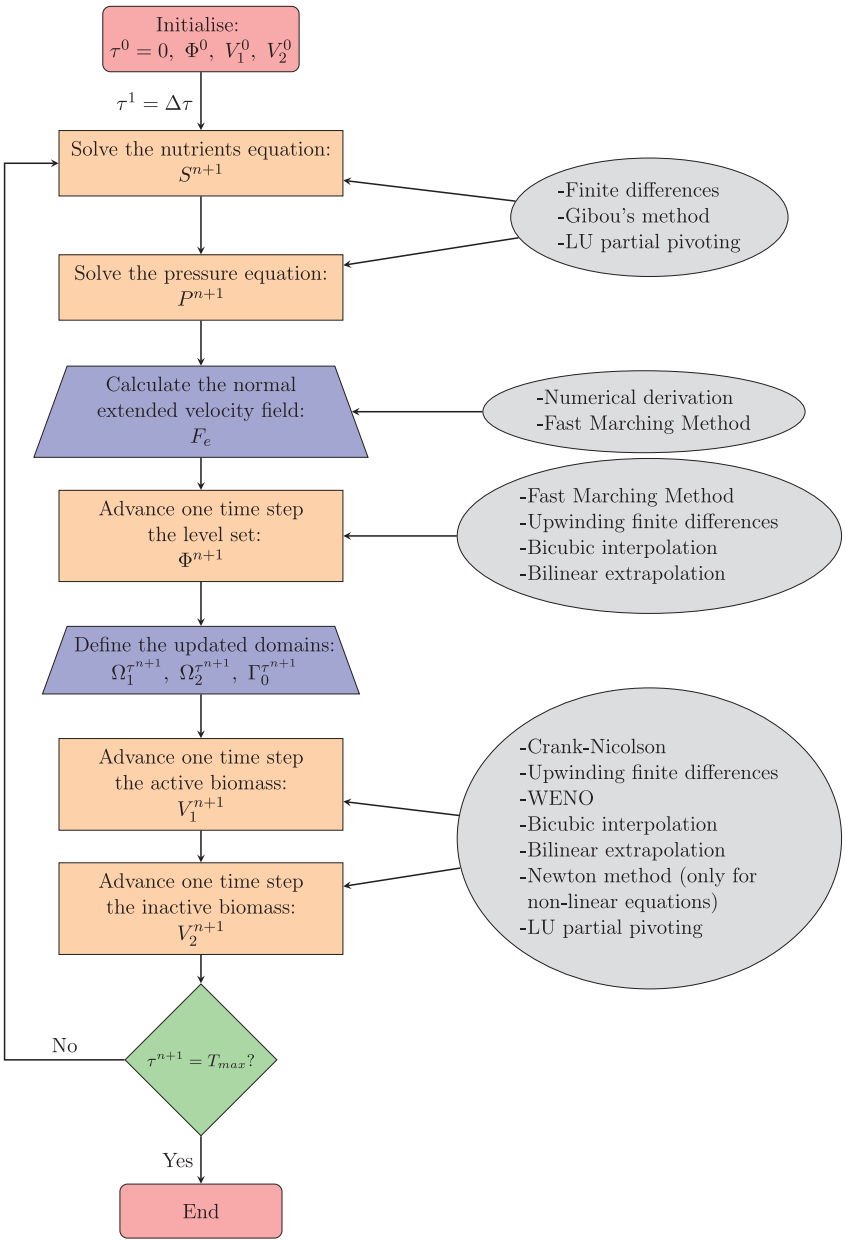

Fig. 3. Flowchart of the global numerical algorithm.

active biomass from the previous iteration (or from the initial condition if we are solving the first iteration), in order to reach the steady-state of the nutrients. Once computed, the new values of the nutrients are used jointly with the values of the biomasses from the previous iteration to solve the pressure equation. The time independence makes the resolution of this equation easier than the biomasses equations.

Nutrients equation is solved in the domain $\Omega^{\tau}_{\hat{H}_B}$, the boundaries of which are Γ_L, Γ_R, Γ_B and $\Gamma^{\tau}_{\hat{H}_b}$. As stated before, the problem conditions grant enough availability of nutrients above $\Gamma^{\tau}_{\hat{H}_b}$, although in the region between $\Gamma^{\tau}_{\hat{H}_b}$ and Γ^{τ}_0 nutrients concentration is affected by the proximity to the biofilm. On the other hand, pressure equation is solved in the domain $\Omega_1^{\tau_n}$, the boundaries of which are Γ_L, Γ_R, Γ_B and $\Gamma_0^{\tau_n}$, as shown in Fig. 2. Above Γ^{τ}_0 there is no presence of biomass, so that the pressure is zero. In both equations the spatial variables are discretised using standard finite differences, modified as in Gibou et al. [16].

Remark 3.1. In order to explain the idea of Gibou's method, let us consider the one dimensional equation

$$u_{xx} = f \text{ in } \Omega = [0, L]. \tag{28}$$

Let $\{x_i\}_{i=0}^{M}$ be the set of nodes of a uniform finite differences mesh of the domain Ω, with $x_0 = 0$, $x_M = L$ and $\Delta x = x_i - x_{i-1}$ constant. Moreover, we denote $u_i \approx u(x_i)$ and $f_i = f(x_i)$. Using a standard finite differences approximation, the discretization of (28) leads to the system of equations:

$$\left[\frac{u_{i+1} - u_i}{\Delta x} - \frac{u_i - u_{i-1}}{\Delta x}\right]\frac{1}{\Delta x} = f_i, \quad \text{for } i = 1, \ldots, M-1. \tag{29}$$

Let us now assume that Ω has a free boundary at $\Gamma = \{x_I\}$ that divides the domain into two disjoint subsets and we know the value $u(x_I) = u_I$. In this setting, we have an index k, such that $x_k \le x_I \le x_{k+1}$. In Gibou's method we use the discretization (29) for $i = 1, \ldots, k-1$. For the node x_k instead of using u_{k+1}, we set an approximation for the ghost node x_{k+1} by using a linear extrapolation as follows:

$$u_{k+1}^G = \frac{u_I + (\theta_k - 1)u_k}{\theta_k}, \quad \text{with } \theta_k = \frac{d(x_k, \Gamma)}{\Delta x} = \frac{|x_I - x_k|}{\Delta x} \in [0, 1]. \tag{30}$$

Note that when θ_k is close to zero, Eq. (30) blows up, so that:

- If $\theta_k \le \Delta x$, we take $u_k = u_I$, where u_I is known.
- Otherwise, the value of the ghost node $u_{k+1} = u_{k+1}^G$ can be used in Eq. (29) for $i = k$, thus obtaining the following second order discretization

$$\left[\frac{u_I - u_k}{\theta_k \Delta x} - \frac{u_k - u_{k-1}}{\Delta x}\right]\frac{1}{\Delta x} = f_k.$$

As u_I is known, it contributes to the second term of the system, so that the final equation for x_k is:

$$-\left(1 + \frac{1}{\theta_k}\right)u_k + u_{k-1} = (\Delta x)^2 f_k - \frac{u_I}{\theta_k}. \tag{31}$$

In a one dimensional domain Ω, the discretization (29) does not cause any further problem. However, in our case, when approaching the boundary $\Gamma_{H_b}^{\tau}$ (or Γ_0^{τ} in the pressure equation), the geometrical aspects related to a two dimensional case make the procedure more complex.

In our cases of nutrients and pressure equations, we choose $\Delta X = \Delta Y$ and the value of θ in Gibou's method depends on the node and the boundary (equation) we are considering. In the case of the nutrients equation, the value of θ at each node is initially given by:

$$\theta_{ij}^S = \frac{d((X_i, Y_j), \Gamma_{H_b}^{\tau})}{\Delta X},$$

while for the pressure equation the value of θ is

$$\theta_{ij}^P = \frac{d((X_i, Y_j), \Gamma_0^{\tau})}{\Delta X}.$$

In our approach, we can take advantage of the level set technique, so that we actually use the expression

$$\theta_{ij}^S = \frac{|\,\phi(X_i, Y_j, \tau^n) - \phi\,|_{\Gamma_{H_b}^{\tau^n}}|}{\Delta X} = \frac{|\,\phi(X_i, Y_j, \tau^n) - H_b\,|}{\Delta X} \tag{32}$$

for the nutrients equation, while we use expression

$$\theta_{ij}^P = \frac{|\,\phi(X_i, Y_j, \tau^n) - \phi\,|_{\Gamma_0^{\tau^n}}|}{\Delta X} = \frac{|\,\phi(X_i, Y_j, \tau^n)\,|}{\Delta X} \tag{33}$$

for the pressure equation.

Let us assume that we are solving the model at time step n+1. Therefore, we need to solve first the nutrients equation

$$-\nabla^2 S^{n+1} = -V_1^n \hat{h}_T^2 S^{n+1}, \text{ in } \Omega_{\hat{H}_B}^{\tau_n}. \tag{34}$$

and then, the pressure equation,

$$-\nabla^2 P^{n+1} = V_1^n \hat{\Psi} S^{n+1} - V_1^n \mathcal{F}_{\mathcal{D}}(V_2^n), \quad \text{in } \Omega_1^{\tau_n}, \tag{35}$$

where

$$\mathcal{F}_{\mathcal{D}}(V_2^n) = \frac{1}{1 + \exp(K_d(D_{min} - mean(V_2^n)))}. \tag{36}$$

If we apply a standard finite differences scheme coupled with Gibou's method [16], the discretization of Eq. (34) leads to the linear system of equations

$$\aleph^n_{S_{i,j+1}} S^{n+1}_{i,j+1} + \aleph^n_{Si+1,j} S^{n+1}_{i+1,j} - \left[\frac{4 + (\theta^S_{ij} - 1)\bar{\aleph}^n_{S_{i,j}}}{\theta^S_{ij}} + (\Delta X)^2 V^n_{1_{i,j}} \hat{h}^2_T \right] S^{n+1}_{i,j} +$$

$$\aleph^n_{S_{i,j-1}} S^{n+1}_{i,j-1} + \aleph^n_{S_{i-1,j}} S^{n+1}_{i-1,j} + \frac{4 - \bar{\aleph}^n_{S_{i,j}}}{\theta^S_{ij}} S^{n+1}_I = 0, \quad \text{if } \aleph^n_{S_{i,j}} = 1, \tag{37}$$

for $i = 0, \ldots, M-1,\ j = 0, \ldots, M$. The term $\aleph^n_{Si,j} = \aleph^n_S(X_i, Y_j)$ is defined in (27), whereas $\bar{\aleph}^n_S$ denotes

$$\bar{\aleph}^n_{S_{i,j}} = \aleph^n_{S_{i,j+1}} + \aleph^n_{S_{i,j-1}} + \aleph^n_{S_{i+1,j}} + \aleph^n_{S_{i-1,j}}, \tag{38}$$

and $S^{n+1}_I = 1$, as stated by the boundary condition (22) for the nutrients concentration on $\Gamma^{\tau_n}_{\hat{H}_b}$.

Note that the value of θ^S_{ij} is given by expression (32). If all neighbouring nodes of (X_i, Y_j) are located bellow the boundary $\Gamma^{\tau_n}_{\hat{H}_b}$ then expression (38) implies that $\bar{\aleph}^n_{S_{i,j}} = 4$, so that the dependence on θ^S_{ij} disappears in the discretized equation for the node (X_i, Y_j) and we recover the standard discretization without ghost node.

In order to establish a linear system involving the value of the nutrients at all mesh nodes, we extend the value $S \equiv 1$ on the boundary $\Gamma^{\tau_n}_{\hat{H}_b}$ to the set $\Omega \backslash \Omega^{\tau_n}_{\hat{H}_b}$. Therefore, we add the following equations

$$S^{n+1}_{i,j} = 1, \quad \text{if } \aleph^n_{S_{i,j}} = 0. \tag{39}$$

The resulting linear system is solved through an LU method with partial pivoting [36].

Once the linear system given by Eqs. (37) and (39) is solved, we proceed to solve the pressure Eq. (35) by applying a standard finite differences scheme coupled with Gibou's method. We obtain the following set of equations:

$$\aleph^n_{i,j+1} P^{n+1}_{i,j+1} + \aleph^n_{i+1,j} P^{n+1}_{i+1,j} - \left[\frac{4 + (\theta^P_{ij} - 1)\bar{\aleph}^n_{i,j}}{\theta^P_{ij}} \right] P^{n+1}_{i,j} +$$

$$\aleph^n_{i,j-1} P^{n+1}_{i,j-1} + \aleph^n_{i-1,j} P^{n+1}_{i-1,j} - (\Delta X)^2 V^n_{1_{i,j}} \left(\mathcal{F}_{\mathcal{D}}(V^n_2) - \hat{\Psi} S^{n+1}_{i,j} \right) = 0, \quad \text{if } \aleph^n_{i,j} = 1, \tag{40}$$

for $i = 0, \ldots, M-1,\ j = 0, \ldots, M$. The term $\aleph^n_{i,j} = \aleph^n(X_i, Y_j)$ is defined in (26), whereas $\bar{\aleph}^n$ denotes

$$\bar{\aleph}^n_{i,j} = \aleph^n_{i,j+1} + \aleph^n_{i,j-1} + \aleph^n_{i+1,j} + \aleph^n_{i-1,j}, \tag{41}$$

Analogously to the nutrients equation, we note that the value of θ^P_{ij} is given by expression (33). Moreover, If all neighbouring nodes of (X_i, Y_j) are located bellow the boundary $\Gamma^{\tau_n}_0$ then expression (41) implies that $\bar{\aleph}^n_{i,j} = 4$, so that the dependence on θ^P_{ij} disappears in the discretized equation for the node (X_i, Y_j) and we recover the standard discretization without ghost node.

Following the steps of Gibou's method, there should be a term P^{n+1}_I, corresponding to the value of the pressure at the interface $\Gamma^{\tau_n}_0$. However, as the boundary conditions state that $P^{n+1}_I = 0$, this term vanishes.

In order to establish a linear system involving the value of the pressure at all mesh nodes, we extend the value $P \equiv 0$ on the boundary $\Gamma^{\tau_n}_0$ to the set $\Omega^{\tau_n}_2$. Therefore, we add the following equation

$$P^{n+1}_{i,j} = 0, \quad \text{if } \aleph^n_{i,j} = 0. \tag{42}$$

The resulting linear system is solved through an LU method with partial pivoting.

3.3. Numerical methods for the level set equation

The level set Eq. (18) describes the evolution of the level set function, Φ, which is used to track the position of the free boundary Γ^{τ}_0 as the zero level set that identifies the boundary of the biofilm domain. Also it allows to identify the boundary $\Gamma^{\tau}_{\hat{H}_b}$. Therefore, the level set equation is part of the numerical strategy to identify the unknown location of changing domains with time and not a proper equation of the model. Introducing the level set equation simplifies the whole numerical solving process, as we can easily describe the solving domains for each equation, without actually locating the position of Γ^{τ}_0 and $\Gamma^{\tau}_{\hat{H}_b}$, for example, or renewing the mesh at every time step.

In order to solve numerically the level set equation, we simply follow the steps of the *Level Set method* as developed in [39], a mathematical tool used to track the movement of free boundaries driven by a certain velocity field. Note that a level set method has also been used in combination with an immersed interphase technique in a Hele-Shaw modelling approach to the biofilm problem in [12]. The method proceeds as follows.

First of all, at the beginning of the numerical solution, the level set function must be appropriately defined by using the initial expression for Γ^0_0. Then, at every time iteration, $n+1$, the following steps are addressed:

1. computation of the expansion growth velocity, $\vec{U}^{n+1}$ at $\Omega_1^{\tau_n}$ by using Eq. (17),
2. computation of the advance normal velocity $F^{n+1} = \vec{U}^{n+1} \cdot \vec{n}$ at the level set $\Gamma_0^{\tau_n}$,
3. extension of the velocity F^{n+1} from $\Gamma_0^{\tau_n}$ to Ω, thus obtaining F_e^{n+1},
4. advance of one time step in the solution of the level set Eq. (18), thus obtaining Φ^{n+1}, by following the steps of the Fast Marching Method [40],
5. reinitialisation of Φ^{n+1} (only when needed).

Once we have done all steps, we get the new level set function, Φ^{n+1} at time τ^{n+1}, that defines solving domains for the system equations, namely $\Omega_1^{\tau_{n+1}}$ and $\Omega_{\hat{H}_b}^{\tau_{n+1}}$. For a complete description of the method, we refer to [8,9,39,40].

The numerical discretization of the level set equation is achieved by using standard upwind finite differences for the spatial derivative and an explicit scheme for the time derivative. Even with the simplicity of the used numerical methods, the discretization is accurate due to other steps of the method. In particular, the construction of the velocity guarantees that the solution of the level set is reliable, provided that we discretise taking into account the direction from which the information is travelling (upwind). Therefore, by applying an explicit scheme for the time derivative we obtain

$$\frac{\Phi^{n+1} - \Phi^n}{\Delta\tau} = -F_e^{n+1} ||\nabla \Phi^n||. \tag{43}$$

Next, by applying an upwinding strategy in space that takes into account the sign of F, we get

$$\Phi_{i,j}^{n+1} = \Phi_{i,j}^n - \Delta\tau F_{e_{i,j}}^n \Big[\max(\text{sign}(F_{e_{i,j}}^n) D_{-X}\Phi_{i,j}^n, -\text{sign}(F_{e_{i,j}}^n) D_{+X}\Phi_{i,j}^n)^2 + \max(\text{sign}(F_{e_{i,j}}^n) D_{-Y}\Phi_{i,j}^n, -\text{sign}(F_{e_{i,j}}^n) D_{+Y}\Phi_{i,j}^n)^2\Big]^{1/2}, \tag{44}$$

where

$$D_{-X}\Phi_{i,j}^n = \frac{\Phi_{i,j}^n - \Phi_{i-1,j}^n}{\Delta X}, \quad D_{+X}\Phi_{i,j}^n = \frac{\Phi_{i+1,j}^n - \Phi_{i,j}^n}{\Delta X},$$
$$D_{-Y}\Phi_{i,j}^n = \frac{\Phi_{i,j}^n - \Phi_{i,j-1}^n}{\Delta Y}, \quad D_{+Y}\Phi_{i,j}^n = \frac{\Phi_{i,j+1}^n - \Phi_{i,j}^n}{\Delta Y}.$$

Once Eq. (44) has been applied at each mesh point, we obtain the values of Φ^{n+1}. With these values we must define the new biofilm domain Ω_1^{n+1}, which is

$$\Omega_1^{\tau_{n+1}} = \{(X,Y) \in \Omega \ / \ \Phi^{n+1}(X,Y) < 0\}.$$

Similarly, the domain $\Omega_2^{\tau_{n+1}}$ is defined as

$$\Omega_2^{\tau_{n+1}} = \{(X,Y) \in \Omega \ / \ \Phi^{n+1}(X,Y) \geq 0\},$$

whereas, the new boundary is

$$\Gamma_0^{n+1} = \partial\Omega_1^{\tau_{n+1}} \cap \partial\Omega_2^{\tau_{n+1}}.$$

Finally, the domain $\Omega_{\hat{H}_b}^{\tau_{n+1}}$ is defined as

$$\Omega_{\hat{H}_b}^{\tau_{n+1}} = \{(X,Y) \in \Omega \ / \ \Phi^{n+1}(X,Y) < \hat{H}_b\},$$

whereas $\Gamma_{\hat{H}_b}^{\tau_{n+1}}$ is

$$\Gamma_{\hat{H}_b}^{\tau_{n+1}} = \{(X,Y) \in \Omega \ / \ \Phi^{n+1}(X,Y) = \hat{H}_b\}.$$

3.4. Numerical methods for the biomasses equations

Both biomasses equations are of advection type. However, the active biomass equation is non-linear. This is the main difference between the numerical strategies used in the active biomass and the rest of the equations of the model, including the inactive biomass. For both biomasses equations we apply Crank-Nicolson [24] for time discretization and an upwinding technique for the spatial discretization, with the upwinding direction determined by the sign of the pressure derivatives.

Moreover, note that due to the application of the Crank-Nicolson method we have an explicit part in which both the pressure and active or inactive biomass spatial derivatives in the previous step are involved, that is ∇P^n and ∇V_1^n in Eq. (19) or ∇P^n and ∇V_2^n in Eq. (20). These derivatives, as well as the term ∇P^{n+1} in the implicit part, are computed by using a WENO scheme [20].

The biomasses equations are solved in the recently computed domain $\Omega_1^{\tau_{n+1}}$, which is bounded by Γ_L, Γ_R, Γ_B and $\Gamma_0^{\tau_{n+1}}$. We first solve the active biomass Eq. (20), which is the next-to-last equation of the model to be solved. At time step $n+1$ we need to compute the values V_1^{n+1}, which represents the approximation of the active biomass at the mesh nodes. For this purpose, by applying a Crank-Nicolson scheme to Eq. (19), we obtain

$$\frac{V_1^{n+1} - V_1^n}{\Delta\tau} = \frac{1}{2}\Big[\nabla P^{n+1} \cdot \nabla V_1^{n+1} + V_1^{n+1}\big(\hat{\Psi} S^{n+1} - (\mathcal{F}_{\mathcal{D}}(V_2^n) + \epsilon_2) - V_1^{n+1}\big(\hat{\Psi} S^{n+1} - \mathcal{F}_{\mathcal{D}}(V_2^n)\big)\big)\Big]$$

$$+\frac{1}{2}\Big[\nabla P^n\cdot\nabla V_1^n+V_1^n\Big(\hat{\Psi}S^n-(\mathcal{F}_{\mathcal{D}}(V_2^n)+\epsilon_2)-V_1^n\Big(\hat{\Psi}S^n-\mathcal{F}_{\mathcal{D}}(V_2^n)\Big)\Big)\Big],\ \text{in } \Omega_1^{\tau_{n+1}},\tag{45}$$

where

$$\mathcal{F}_{\mathcal{D}}(V_2^n)=\frac{1}{1+\exp(K_d(D_{min}-mean(V_2^n)))}.$$

In order to establish a linear system involving the value of the biomass at all mesh nodes, we extend the value $V_1\equiv 0$ on the boundary $\Gamma_0^{\tau_{n+1}}$ to the set $\Omega_2^{\tau_{n+1}}$. Therefore, we add the following equation

$$V_1^{n+1}=0,\quad \text{in } \Omega_2^{\tau_{n+1}}.\tag{46}$$

Note that $P^n, P^{n+1}, S^n, S^{n+1}$ and V_1^n are all known values. The decay term $\mathcal{F}_{\mathcal{D}}$ is a function that depends on the mean concentration of inactive biomass. In order to decrease the difficulty of the problem, instead of considering the mean inactive biomass of the current iteration, we use the mean inactive biomass from the previous iteration, V_2^n, so that $mean(V_2^n)$ is also a known value. In order to compute $\nabla P^{n+1}, \nabla P^n$ and ∇V_1^n we use a WENO scheme, while to discretise ∇V_1^{n+1} we use an upwind strategy, so that Eq. (45) results into:

$$\begin{aligned}V_{1_{i,j}}^{n+1}-\frac{1}{2}\Delta\tau\Bigg[&\max(P_X^{n+1},0)\frac{V_{1_{i+1,j}}^{n+1}-V_{1_{i,j}}^{n+1}}{\Delta X}+\min(P_X^{n+1},0)\frac{V_{1_{i,j}}^{n+1}-V_{1_{i-1,j}}^{n+1}}{\Delta X}+\\&\max(P_Y^{n+1},0)\frac{V_{1_{i,j+1}}^{n+1}-V_{1_{i,j}}^{n+1}}{\Delta Y}+\min(P_Y^{n+1},0)\frac{V_{1_{i,j}}^{n+1}-V_{1_{i,j-1}}^{n+1}}{\Delta Y}+\\&V_{1_{i,j}}^{n+1}\Big(\hat{\Psi}S_{i,j}^{n+1}-(\mathcal{F}_{\mathcal{D}}(V_2^n)+\epsilon_2)\Big)-(V_{1_{i,j}}^{n+1})^2\Big(\hat{\Psi}S_{i,j}^{n+1}-\mathcal{F}_{\mathcal{D}}(V_2^n)\Big)\Bigg]-\\&\frac{1}{2}\Delta\tau\Big[\nabla P_{i,j}^n\cdot\nabla V_{1_{i,j}}^n+V_{1_{i,j}}^n\Big(\hat{\Psi}S_{i,j}^n-(\mathcal{F}_{\mathcal{D}}(V_2^n)+\epsilon_2)\Big)-\\&(V_{1_{i,j}}^n)^2\Big(\hat{\Psi}S_{i,j}^n-\mathcal{F}_{\mathcal{D}}(V_2^n)\Big)\Big]-V_{1_{i,j}}^n=0,\quad \text{if } \aleph_{i,j}^{n+1}=1,\end{aligned}\tag{47}$$

whereas Eq. (46) becomes

$$V_{1_{i,j}}^{n+1}=0,\quad \text{if } \aleph_{i,j}^{n+1}=0,\tag{48}$$

for $i=0,\dots,M-1,\ j=0,\dots,M$. For the purpose of clarity, let us introduce the following notation

$$P_{X_{i,j}}^{+}=\max(P_X^{n+1},0),\quad P_{Y_{i,j}}^{+}=\max(P_Y^{n+1},0),\tag{49}$$

$$P_{X_{i,j}}^{-}=\min(P_X^{n+1},0),\quad P_{Y_{i,j}}^{-}=\min(P_Y^{n+1},0),\tag{50}$$

$$\alpha_1=\frac{\Delta\tau}{2\Delta X}=\frac{\Delta\tau}{2\Delta Y}\quad \text{(as we choose } \Delta X=\Delta Y),\tag{51}$$

$$\theta_{i,j}^k\equiv\theta(S_{i,j}^k)=\hat{\Psi}S_{i,j}^k-\mathcal{F}_{\mathcal{D}}(V_2^n),\ \text{with } k=n,n+1,\tag{52}$$

$$\sigma_{i,j}^k\equiv\sigma(S_{i,j}^k)=\hat{\Psi}S_{i,j}^k-\mathcal{F}_{\mathcal{D}}(V_2^n)-\epsilon_2,\ \text{with } k=n,n+1,\tag{53}$$

$$g_{i,j}^n\equiv g(P_{i,j}^n,V_{1_{i,j}}^n)=\nabla P_{i,j}^n\cdot\nabla V_{1_{i,j}}^n+V_{1_{i,j}}^n\sigma_{i,j}^n-(V_{1_{i,j}}^n)^2\theta_{i,j}^n,\tag{54}$$

$$\delta_{i,j}^{n+1}=1+\alpha_1P_{X_{i,j}}^{+}-\alpha_1P_{X_{i,j}}^{-}+\alpha_1P_{Y_{i,j}}^{+}-\alpha_1P_{Y_{i,j}}^{-}-\alpha_1\Delta XV_{1_{i,j}}^{n+1}\sigma_{i,j}^{n+1}.\tag{55}$$

Then, the system of Eqs. (47) and (48) can be written in equivalent form

$$\begin{aligned}&-\alpha_1P_{X_{i,j}}^{+}V_{1_{i+1,j}}^{n+1}-\alpha_1P_{Y_{i,j}}^{+}V_{1_{i,j+1}}^{n+1}+\delta_{i,j}^{n+1}V_{1_{i,j}}^{n+1}\\&+\alpha_1\Delta X(V_{1_{i,j}}^n)^2\theta_{i,j}^{n+1}+\alpha_1P_{X_{i,j}}^{-}V_{1_{i-1,j}}^{n+1}+\alpha_1P_{Y_{i,j}}^{-}V_{1_{i,j-1}}^{n+1}\\&-\alpha_1g_{i,j}^n-V_{1_{i,j}}^n=0,\quad \text{if } \aleph_{i,j}^{n+1}=1,\end{aligned}\tag{56}$$

$$V_{1_{i,j}}^{n+1}=0,\quad \text{if } \aleph_{i,j}^{n+1}=0,\tag{57}$$

for $i=0,\dots,M-1,\ j=0,\dots,M$. Thus, we end up obtaining the non-linear system of Eqs. (56) and (57) that can be solved by a Newton method. At each Newton iteration, an LU method with partial pivoting is applied to the resulting linear system.

At step $n+1$, we finally need to compute the values V_2^{n+1}, which represent the approximation of the inactive biomass at the mesh nodes, by solving the inactive biomass equation. In order to do so, we apply a Crank-Nicolson scheme for time discretization to (20), thus obtaining

$$\frac{V_2^{n+1}-V_2^n}{\Delta\tau} = \frac{1}{2}\Big[\nabla P^{n+1}\cdot\nabla V_2^{n+1} + V_1^{n+1}\epsilon_2 - V_2^{n+1}\big(V_1^{n+1}\hat{\Psi}S^{n+1} - V_1^{n+1}\mathcal{F}_{\mathcal{D}}(V_2^n)\big)\Big] + \frac{1}{2}\Big[\nabla P^{n}\cdot\nabla V_2^{n} + V_1^{n}\epsilon_2 - V_2^{n}\big(V_1^{n}\hat{\Psi}S^{n} - V_1^{n}\mathcal{F}_{\mathcal{D}}(V_2^n)\big)\Big], \quad \text{in } \Omega_1^{\tau_{n+1}}, \tag{58}$$

where

$$\mathcal{F}_{\mathcal{D}}(V_2^n) = \frac{1}{1+\exp(K_d(D_{min}-mean(V_2^n)))}.$$

In order to establish a linear system involving the value of the biomass at all mesh nodes, we extend the value $V_2 \equiv 0$ on the boundary $\Gamma_0^{\tau_{n+1}}$ to the set $\Omega_2^{\tau_{n+1}}$. Therefore, we add the following equations

$$V_2^{n+1} = 0, \quad \text{in } \Omega_2^{\tau_{n+1}}. \tag{59}$$

Note that the values $P^n, P^{n+1}, V_1^n, V_1^{n+1}, S^n, S^{n+1}$ and V_2^n are all known, and therefore $mean(V_2^n)$ is known as well. For the computation of $\nabla P^{n+1}, \nabla P^n$ and ∇V_2^n we use a WENO method. Finally, in order to discretise ∇V_2^{n+1} we use an upwind strategy. The discretization of (58) results as follows:

$$V_{2_{i,j}}^{n+1} - \frac{1}{2}\Delta\tau\Bigg[\max(P_X^{n+1},0)\frac{V_{2_{i+1,j}}^{n+1}-V_{2_{i,j}}^{n+1}}{\Delta X} + \min(P_X^{n+1},0)\frac{V_{2_{i,j}}^{n+1}-V_{2_{i-1,j}}^{n+1}}{\Delta X} + \max(P_Y^{n+1},0)\frac{V_{2_{i,j+1}}^{n+1}-V_{2_{i,j}}^{n+1}}{\Delta Y} + \min(P_Y^{n+1},0)\frac{V_{2_{i,j}}^{n+1}-V_{2_{i,j-1}}^{n+1}}{\Delta Y} + V_{1_{i,j}}^{n+1}\epsilon_2 - V_{2_{i,j}}^{n+1}V_{1_{i,j}}^{n+1}\big(\hat{\Psi}S_{i,j}^{n+1} - \mathcal{F}_{\mathcal{D}}(V_2^n)\big)\Bigg] - \frac{1}{2}\Delta\tau\Big[\nabla P_{i,j}^n\cdot\nabla V_{2_{i,j}}^n + V_{1_{i,j}}^n\epsilon_2 - V_{2_{i,j}}^n V_{1_{i,j}}^n\big(\hat{\Psi}S_{i,j}^n - \mathcal{F}_{\mathcal{D}}(V_2^n)\big)\Big] - V_{2_{i,j}}^n = 0, \quad \text{if } \aleph_{i,j}^{n+1} = 1, \tag{60}$$

whereas Eq. (59) becomes

$$V_{2_{i,j}}^{n+1} = 0, \quad \text{if } \aleph_{i,j}^{n+1} = 0, \tag{61}$$

for $i = 0,\dots,M-1,\ j = 0,\dots,M$. Next, we use the notation defined in (49)–(51) with the following modifications to (52), (54) and (55):

$$\theta_{i,j}^k \equiv \theta(S_{i,j}^k) = \hat{\Psi}S_{i,j}^k - \mathcal{F}_{\mathcal{D}}(V_2^n), \ \text{ with } k = n, n+1, \tag{62}$$

$$g_{i,j}^n \equiv g(P_{i,j}^n, V_{1_{i,j}}^n, V_{2_{i,j}}^n) = \nabla P_{i,j}^n\cdot\nabla V_{2_{i,j}}^n + V_{1_{i,j}}^n\epsilon_2 - V_{2_{i,j}}^n V_{1_{i,j}}^n\theta_{i,j}^n, \tag{63}$$

$$\delta_{i,j}^{n+1} = 1 + \alpha_1 P_{X_{i,j}}^+ - \alpha_1 P_{X_{i,j}}^- + \alpha_1 P_{Y_{i,j}}^+ - \alpha_1 P_{Y_{i,j}}^- + \alpha_1\Delta X V_{1_{i,j}}^{n+1}\theta_{i,j}^{n+1}. \tag{64}$$

Then, the system of Eqs. (60) and (61) can be written in the following equivalent form:

$$-\alpha_1 P_{X_{i,j}}^+ V_{2_{i+1,j}}^{n+1} - \alpha_1 P_{Y_{i,j}}^+ V_{2_{i,j+1}}^{n+1} + \delta_{i,j}^{n+1}V_{2_{i,j}}^{n+1} + \alpha_1 P_{X_{i,j}}^- V_{2_{i-1,j}}^{n+1} + \alpha_1 P_{Y_{i,j}}^- V_{2_{i,j-1}}^{n+1} - \alpha_1 g_{i,j}^n - \alpha_1\Delta X V_{1_{i,j}}^{n+1}\epsilon_2 - V_{2_{i,j}}^n = 0, \quad \text{if } \aleph_{i,j}^{n+1} = 1 \tag{65}$$

$$V_{2_{i,j}}^{n+1} = 0, \quad \text{if } \aleph_{i,j}^{n+1} = 0. \tag{66}$$

for $i = 0,\dots,M-1,\ j = 0,\dots,M$. An LU method with partial pivoting is applied to the linear system.

4. Description and discussion of numerical tests

Various recent works considered the spatial characterisation of *L. monocytogenes* biofilms at different times using microscopy and image analysis. For example, Rieu et al. [37] presented a comparison of biovolume and mean thickness for *L. monocytogenes* biofilms under batch and flow conditions using CLSM and PHLIP. Bridier et al. [6] quantified maximum thickness, biovolume and roughness using PHLIP for biofilms formed by 10 different *L. monocytogenes* strains at 24 h. Similarly, Guilbaud et al. [17] studied the structural diversity of biofilms formed by 96 *L. monocytogenes* strains at 48 h using also mean thickness, biovolume and roughness. Mosquera et al. [30] considered the dynamics of the structure of different strains throughout their life cycle.

Table 2
Parameters values used in the numerical tests. Note that μ and k_i take different values depending on the considered case: a-e and I-III, respectively.

Parameter	Value	Unit
L, H	3×10^{-4}	m
H_b	0.125H	m
ρ	17	kg/m^3
D	2.568×10^{-12}	m^2/s
γ	0.98	-
μ	a) 4.25×10^{-5}; b) 1.7×10^{-4}; c) 8.5×10^{-4}; d) 1.7×10^{-3}; e) 8.5×10^{-3}	s^{-1}
K_d	311.5	-
D_{min}	5.21×10^{-2}	-
k_i	(I) 8.95×10^{-8}; (II) 1.0×10^{-6}; (III) 1.0×10^{-5}	s^{-1}
t_D	86400	s
s^*	2.74	kg/m^3

Those works reveal that biofilms at early times form small joint or separated clusters. As the biofilm evolves, larger biofilms appear which may present various different structures: mono-layers of adhered cells, flat unstructured multi-layers, honeycomb structures or large clusters [6,7,14,26,35,37].

Here we use the model to analyse the roles of the initial conditions (joint or separated clusters), the bacterial maximum growth rate and the inactivation rate on the development of different structures in *L. monocytogenes* biofilms. As we aim to validate the model and the numerical methods with real-world cases taken from the laboratory, we consider data from the experiments in [4] and try to reproduce the observed results therein.

We label the numerical tests as **T1** for those cases in which the initial conditions correspond to joint clusters:

$$\Gamma_0^0 = \{(X,Y) \in \Omega / Y = 0.2 + 0.05\sin(4\pi X)\}, \tag{67}$$

$$\Omega_1^0 = \{(X,Y) \in \Omega / Y < 0.2 + 0.05\sin(4\pi X)\}, \tag{68}$$

$$V_1(X,Y,0) = 1, \quad V_2(X,Y,0) = 0, \ \text{in } \Omega_1^0. \tag{69}$$

and **T2** for those cases in which the initial conditions correspond to separated clusters:

$$\Gamma_{0,a}^0 = \{(X,Y) \in \Omega / X < 0.5, Y = -0.3565 + 0.6065 * \sin(2\pi X)\},$$
$$\Gamma_{0,b}^0 = \{(X,Y) \in \Omega / X \geq 0.5, Y = -0.3565 + 0.6065 * \sin(2\pi (X - 0.5))\},$$
$$\Omega_{0,a}^0 = \{(X,Y) \in \Omega / X < 0.5, Y < -0.3565 + 0.6065 * \sin(2\pi X)\},$$
$$\Omega_{0,b}^0 = \{(X,Y) \in \Omega / X \geq 0.5, Y < -0.3565 + 0.6065 * \sin(2\pi (X - 0.5))\},$$

where $\Gamma_0^0 = \Gamma_{0,a}^0 \cup \Gamma_{0,b}^0$ and $\Omega_0^0 = \Omega_{0,a}^0 \cup \Omega_{0,b}^0$.

As stated in Section 1, the sensitivity analysis of the parameters has been addressed in [4]. From this analysis, it follows that the most relevant parameters involved in the growth of a Listeria biofilm are the maximum growth rate, μ, and the inactivation rate, k_i. The following Table 2 presents the parameter values as adapted from [4].

4.1. Flat or rough L. monocytogenes *biofilms*

Visual inspection of the biofilms formed by the *L. monocytogenes* strain L1A1 reveals the presence of thick almost flat biofilms, as illustrated by Fig. 2 in [4], where the three-dimensional reconstruction of the CLSM images captured at different times of the biofilms life cycle is presented. The images at earlier times show the presence of small clusters, which eventually joined to each other in a honeycomb pattern. Later this pattern disappears to form an unstructured flat mass.

L1A1 is not the only strain that develops flat or rough structures. Guilbaud et al. [17] observed that *L. monocytogenes* strains without flagellum developed flat structures at 48 h. Some examples include CIP 82110 (a virulent type strain from rabbit), LM 6298 (from soil) or H6 (from a healthy 30-year-old woman) strains. PilchovÃ!‘ et al. [35] studied structures at 1, 3 and 6 days and suggested that the EGD-e strain isolated from listeriosis outbreaks could skip the honeycomb-like pattern during the life cycle, evolving to flat structures.

In this work we used the proposed model to explore the role of the initial conditions, the growth rate and the inactivation rate into the formation of flat or rough structures. Figs. 4 and 5 present the dynamics of two particular cases: T1bI and T1bIII, which would correspond to a couple of cases in which joint clusters evolve to form flat or rough structures.

In Fig. 4 the model rapidly evolves to a dense flat biofilm with a maximum thickness of 0.76. Inactivation is very low and the biofilm grows till nutrients are consumed. In Fig. 5 damaged cells slowly appear in the deepest layers of the biofilm thus evolving toward a multi-layered practically flat biofilm as the ones observed for L1A1 [30]. Note that the detachment induced by the presence of damaged cells sets the maximum thickness to a value of 0.64.

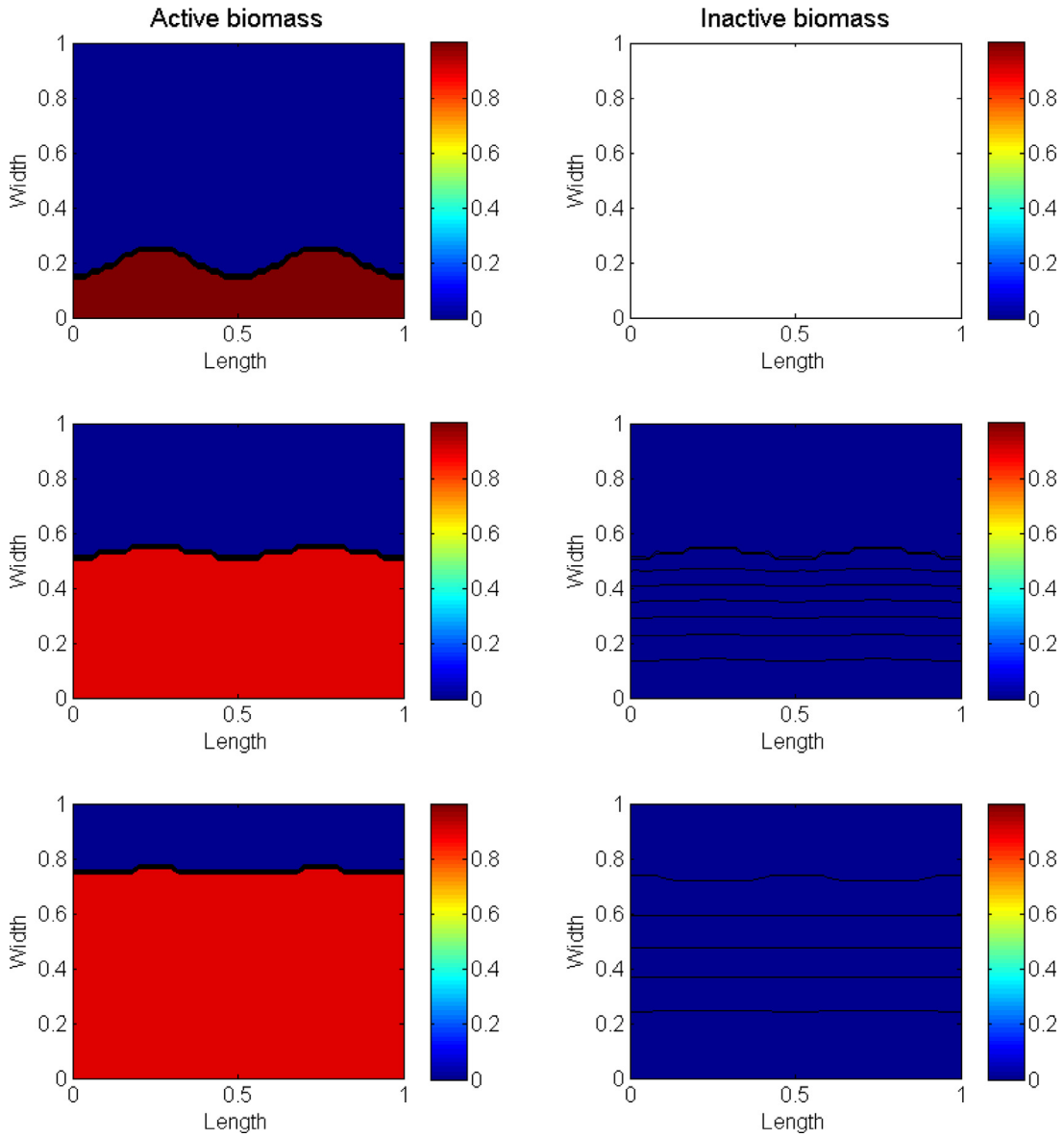

Fig. 4. Case T1bI: $\mu = 1.7 \times 10^{-4}$; $k_i = 8.95 \times 10^{-8}$. Left column shows active biomass, right column shows inactive biomass. First row presents the initial conditions, while second and third rows show the biomasses after 5.76h and 9.6h, respectively. Two joint clusters evolve toward a thick flat structure in absence of damaged or dead cells.

The question is now whether initially separated clusters can evolve to form flat biofilms as well. Fig. 6 shows that it is indeed the case. Remarkably, this may happen for those strains in which the growth rate is within the lower range and independently of the presence of damaged cells which will only affect the final thickness and roughness.

Figures show that flat structures may appear regardless the initial conditions. However, final thickness is clearly affected by the presence of joint or separated clusters at early times. In the case of separated clusters the biofilm grows horizontally and vertically, while in the case of joint clusters, it evolves to thicker biofilms. Cases T1bI in Fig. 4 - with a maximum thickness of 0.76 - and T2bI in Fig. 6 - with a maximum thickness of 0.63 - clearly illustrate this issue.

These profiles can be directly compared to those ones depicted for L1A1 in [4] and CIP 82110, LM6298 or H6 in Guilbaud et al. [17].

4.2. Complex structures: clusters, honeycomb and mushrooms

Bridier et al. [6] observed that several *L. monocytogenes* strains produced biofilms containing several small clusters of variable thickness in static cultures at 24h. Mosquera et al. [30] also reported the presence of clusters at early stages of

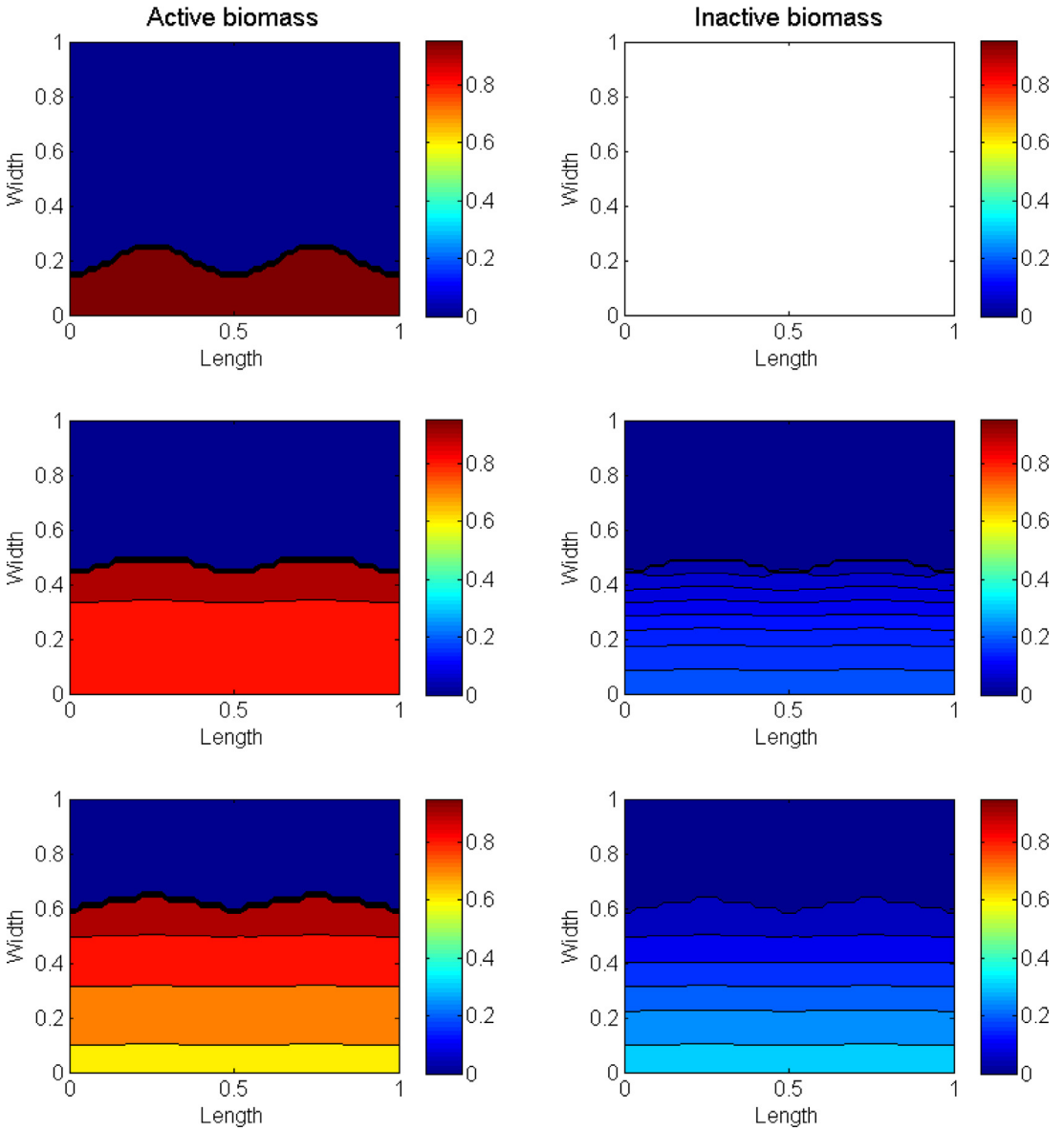

Fig. 5. Case T1bIII: $\mu = 1.7 \times 10^{-4}$; $k_i = 1 \times 10^{-5}$. Left column shows active biomass, right column shows inactive biomass. First row presents the initial conditions, while second and third rows show the biomasses after 5.76h and 9.6h, respectively. Two joint clusters evolve toward a multi-layered flat structure with the presence of damaged or dead cells in deep layers.

biofilm formation for the strains CECT 4032 and CECT 5873. At later stages, these clusters may join to each other and form honeycomb patterns with small channels or even voids such as those ones observed by Guilbaud et al. [17], Picholva et al. [35] or Mosquera et al. [30].

Note that Fig. 3 in Mosquera et al. [30] shows the CLSM reconstructions at different times for the strain CECT 5873. This figure illustrates the presence of multiple microcolonies or small clusters at the initial time. Those clusters evolve to form larger clusters which eventually disappear to form an unstructured flatter biofilm once the amount of inert biomass is substantial.

Again we explored the conditions for which the proposed model is able to depict this type of more complex structures by playing around with the initial conditions, the growth and inactivation rates. Figs. 7 and 8 present the dynamics of two particular cases: T2cI and T2cIII, which would correspond to a couple of examples in which separated clusters evolve to form complex structures.

In Figs. 7 and 9 (first row) the model shows how initially separated clusters rapidly evolve till they practically join each other leaving open channels in the deepest layers of the biofilm. The maximum thickness would correspond to a value of 0.74. Inactivation is not significant and clusters are dense. On the contrary, Fig. 8 shows a significant presence of

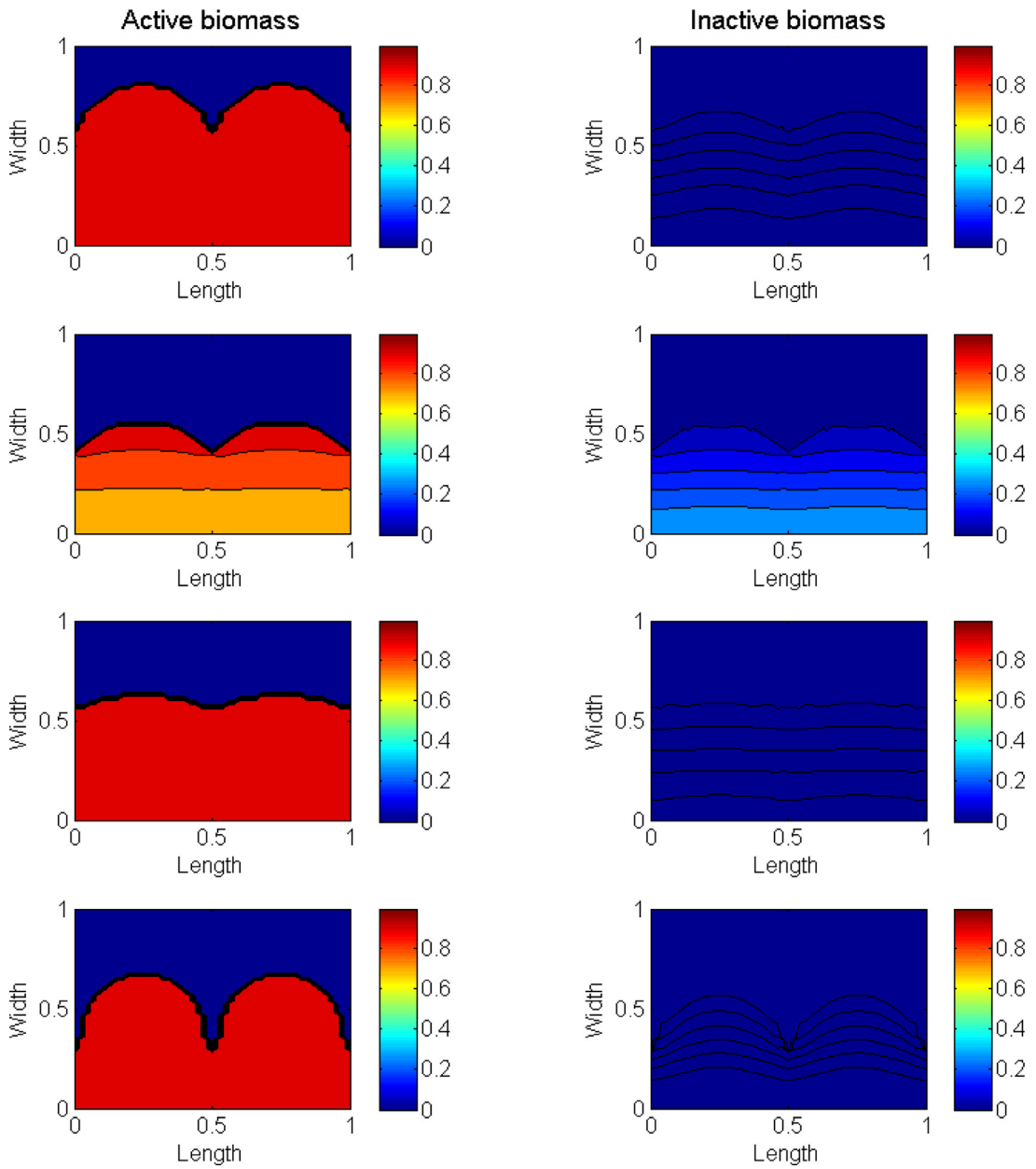

Fig. 6. Final simulation time flat or rough structures. Each row corresponds to the cases: T1cI, T2bIII, T2bI, T1eI.

damaged cells which induce a strong detachment process leading to the formation of mushroom type structures. Note that the maximum thickness would be 0.61. Mushrooms are stratified with a substantial amount of damaged cells in the lower layers.

Remarkably, if the growth rate is higher and the inactivation rate is lower then separated clusters tend to evolve as separated dense clusters (see Fig. 9, second row). Thus certain inactivation, in other words detachment, is required for the clusters to join each other.

The question is now whether initially joint clusters can evolve to form complex structures as the ones showed in previous figures. Fig. 9 shows that it is indeed the case. In fact, this may happen for those strains in which the growth rate is within the upper range.

Results reveal that the larger growth rate contributes to forming thick clusters while the lower inactivation rate contributes to slowing down the detachment. As an overall effect, dense clusters are observed in which channels are formed due to the slow superficial detachment. Again inert biomass tends to accumulate inside the clusters, as it can also be observed in the CLSM reconstructions in Fig. 3 in Mosquera et al. [30].

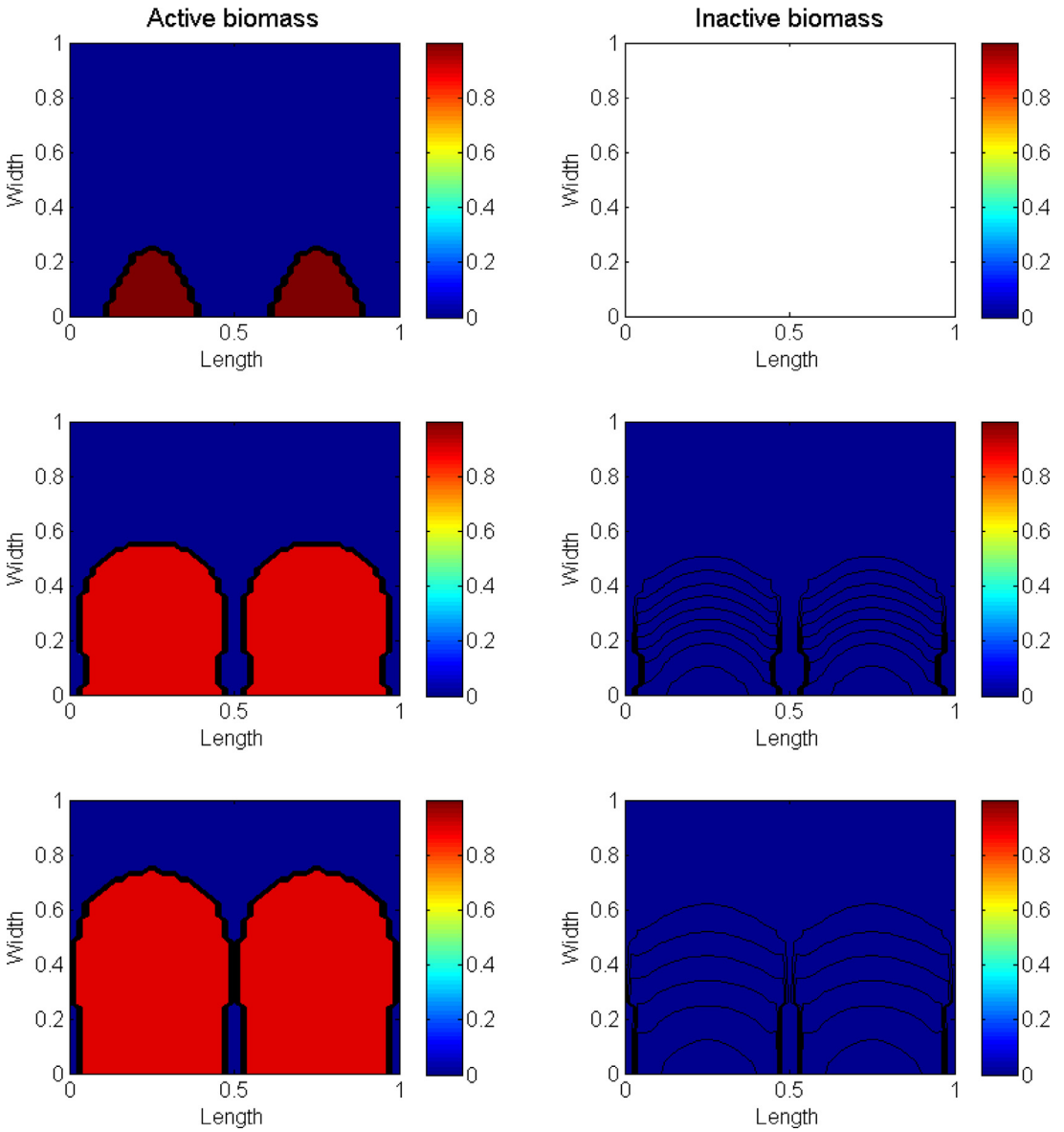

Fig. 7. Case T2cI: $\mu = 1.7 \times 10^{-3}$; $k_i = 8.95 \times 10^{-8}$. Left column shows active biomass, right column shows inactive biomass. First row presents the initial conditions, while second and third rows show the biomasses after 5.76h and 9.6h, respectively. Two separated clusters evolve toward a thick honeycomb type structure in absence of damaged or dead cells.

All in all, our simulation results show that the proposed 2-D multi-species model is able to qualitatively predict the interstrain variability found in *L. monocytogenes* biofilms. Initial attachment (initial conditions), and detachment rate (which relates to inactive biomass), condition the development of flat, clustered or honeycomb type structures.

5. Conclusions

Listeria monocytogenes is addressed as a high-risk bacteria, specially relevant in food industry. This pathogen develops biofilms in common food contact surfaces and has a great tolerance to biocides, thus persisting despite the sanitising efforts. Therefore, the study of *L. monocytogenes* biofilms is of the utmost importance. This study can be based on experiments in laboratory or in mathematical modelling tool, as well as on the combination of both.

In this work, a new two-dimensional deterministic mathematical model is proposed to reproduce the variability of strain structures observed in laboratory. The model is mainly based on the work of Alpkvist and Klapper [1] and adequately modified following the insights obtained by Balsa-Canto et al. [4]. The proposed model consists in a set of coupled partial differential equations and considers the nutrients concentration and the active and inactive biomasses concentrations. Several key

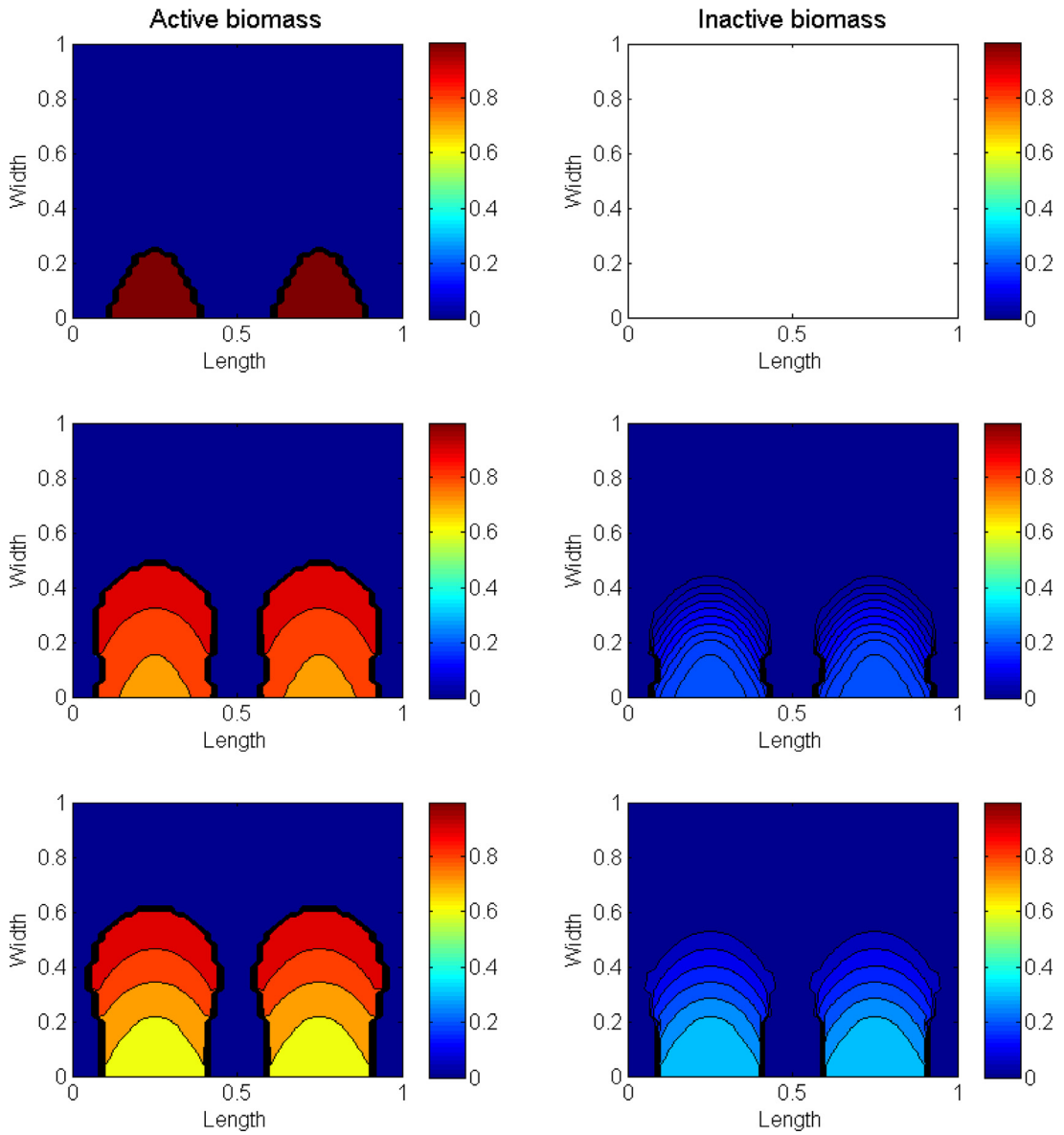

Fig. 8. Case T2cIII: $\mu = 1.7 \times 10^{-3}$; $k_i = 1 \times 10^{-5}$. Left column shows active biomass, right column shows inactive biomass. First row presents the initial conditions, while second and third rows show the biomasses after 5.76h and 9.6h, respectively. Two separated clusters evolve toward a mushroom type structure with the presence of damaged or dead cells in deep layers of the mushrooms.

mechanisms that determine the dynamics of *L. monocytogenes* biofilms are included, in particular the mass action law that describes a home made nutrients uptake and biomass growth, as well as a non-linear detachment to account for the ageing mechanism. The mathematical analysis of the model to obtain the existence and uniqueness of solution in the appropriate functional spaces requires further studies. As it is not possible to obtain an analytical solution for the proposed highly non-linear coupled model, it is solved by using highly-efficient numerical methods that guarantee the robustness and stability of the solution. These appropriate numerical techniques include the Level Set method, WENO methods, a Crank-Nicolson scheme and a Newton method, among others. Although separately, they mostly consist of standard numerical methods, their implementation from scratch for our complex coupled model results challenging. Also a rigorous numerical analysis to theoretically establish convergence and stability properties of the combination of the methods to solve the coupled model is an open question for future research.

We have validated our model by comparing simulation results with real biofilms dynamics as obtained in the laboratory. All things considered, the obtained numerical results allow to reproduce several different behaviours showed by various *L. monocytogenes* strains. In Section 4.1, a case is proposed where the biofilm develops a flat structure, such as the ones exhibited by the L1A1 strain. Numerical results are in high agreement with the experimental ones obtained in the laboratory,

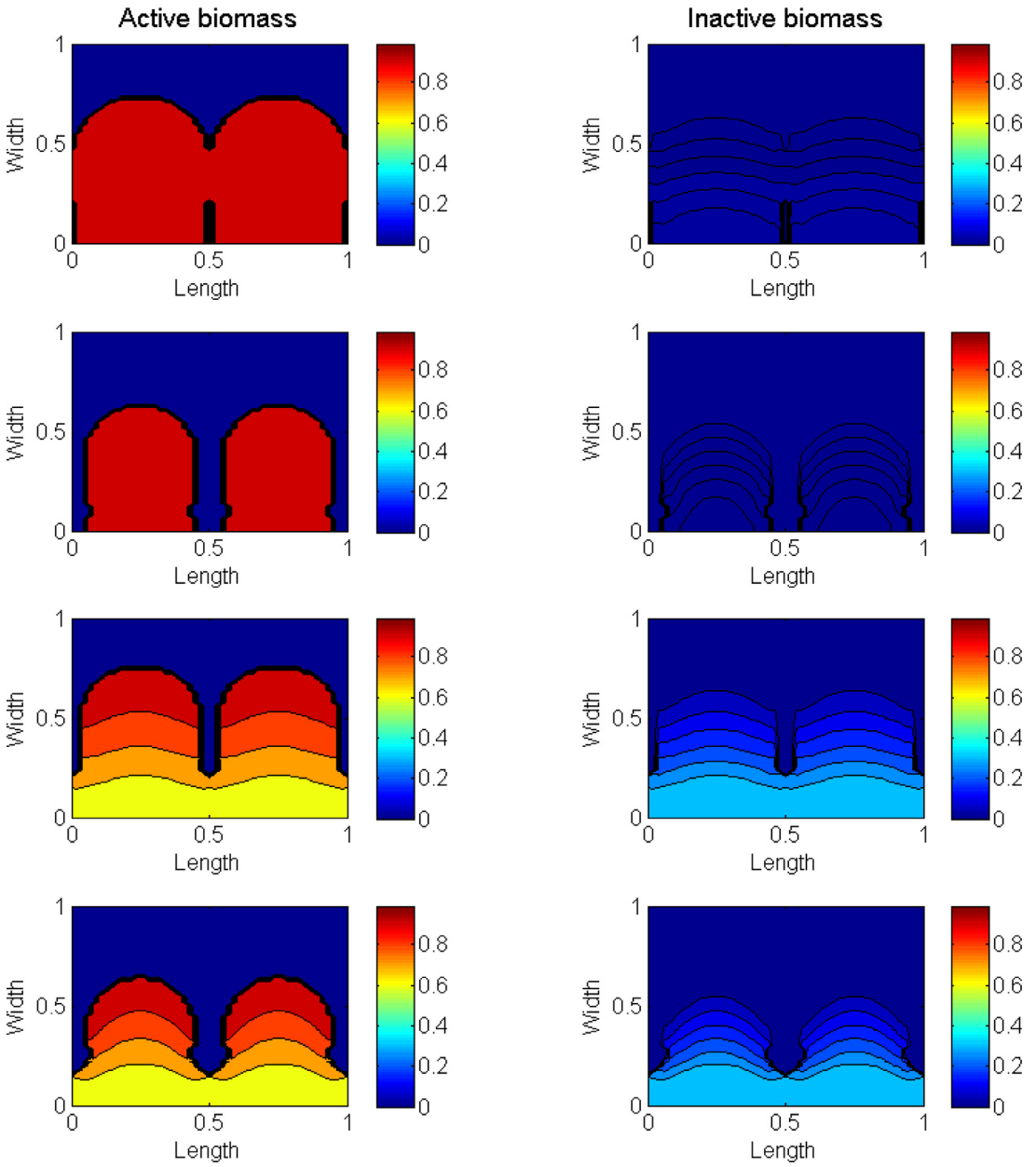

Fig. 9. Final simulation time complex structures. Each row corresponds to the cases: T2dII, T2dI, T1cIII, T1eIII.

thus confirming the capabilities of the model. Moreover, in Section 4.2 two additional different cases are depicted that account for the behaviour of CECT 4032 and CECT 5873 strains: a clustered biofilm formation and honeycomb structures.

The fact that our model is able to explain the dynamics of different structures is an important contribution of the present work. Although the study focuses on a number of *L. monocytogenes* strains our model and numerical approaches may well apply to other species.

References

[1] E. Alpkvist, I. Klapper, A multidimensional multispecies continuum model for heterogeneous biofilm development, Bull. Math. Biol. 69 (2007) 765–789.
[2] E. Alpkvist, C. Picioreanu, M.C.M. van Loosdrecht, A. Heyden, Three-dimensional biofilm model with individual cells and continuum EPS matrix, Biotechnol. Bioeng. 94 (2006) 961–979.
[3] E. Balsa-Canto, A. López-Núñez, C. Vázquez, Numerical methods for a reaction-diffusion system modelling biofilm formation, Appl. Math. Model. 41 (2017) 164–179.
[4] E. Balsa-Canto, C. Vilas, A. López-Núñez, M. Mosquera-Fernández, R. Briandet, M.L. Cabo, C. Vázquez, Modeling reveals the role of aging and glucose uptake impairment in l1a1 *Listeria monocytogenes* biofilm life cycle, Front. Microbiol. 8 (2017) 2118.

[5] H. Beyenal, Z. Lewandowski, G. Harkin, Quantifying biofilm structure: facts and fiction, Biofouling 20 (2004) 1–23.
[6] A. Bridier, F. Dubois-Brissonnet, A. Boubetra, V. Thomas, R. Briandet, The biofilm architecture of sixty opportunistic pathogens deciphered using a high throughput CLSM method, J. Microbiol. Methods 82 (2010) 64–70.
[7] M.S. Chae, H. Schraft, Comparative evaluation of adhesion and biofilm formation of different *Listeria monocytogenes* strains, Int. J. Food Microbiol. 62 (2000) 103–111.
[8] D.L. Chopp, Another look at velocity extensions in the level set method, SIAM J. Scientif. Comput. 31 (2009) 3255–3273.
[9] D.L. Chopp, Numerical methods for moving interfaces, 2017, (????). ESAM 449 Course Notes.
[10] B. Carpentier, P. Cerf, Persistence of *Listeria monocytogenes* in food industry equipment and premises, Int. J. Food Microbiol. 145 (2011) 1–8.
[11] P. Cossart, A. Lebreton, A trip in the 'new microbiology' with the bacterial pathogen *Listeria monocytogenes*, FEBS Lett. 588 (2014) 2437–2445.
[12] P. Cumsille, J.A. Asenjo, C. Conca, A novel model for biofilm growth and its resolution by using the hybrid immersed interface-level set method, Comput. Math. Appl. 67 (2014) 34–51.
[13] H. Daims, M. Wagner, Quantification of uncultured microorganisms by fluorescence microscopy and digital image analysis, Appl. Microbiol. Biotechnol. 75 (2007) 237–248.
[14] D. Djordjevic, M. Wiedmann, L. McLandsborough, Microtiter plate assay for assessment of *Listeria monocytogenes* biofilm formation, Appl. Environ. Microbiol. 68 (2002) 2950–2958.
[15] J.D. Dockery, I. Klapper, Finger formation in biofilm layers, SIAM J. Appl. Math. 62 (2001) 853–869.
[16] F. Gibou, R. Fedkiw, L.T. Cheng, M. Kang, A second order accurate symmetric discretization of the poisson equation on irregular domains, J. Comput. Phys. 176 (2002) 205–227.
[17] M. Guilbaud, P. Piveteau, M. Desvaux, S. Brisse, R. Briandet, Exploring the diversity of *Listeria monocytogenes* biofilm architecture by high-throughput confocal laser scanning microscopy and the predominance of the honeycomb-like morphotype, Appl. Environ. Microbiol. 81 (2015) 1804–1810.
[18] A. Heydorn, A.T. Nielsen, M. Hentzer, C. Sternberg, M. Givskov, B.K. Ersboll, Quantification of biofilm structures by the novel computer program COMSTAT, Microbiology 146 (2000) 2395–2407.
[19] S. Hunt, M.H. S, J. Sears, G. Harkin, J. Reno, A computer investigation of chemically mediated detachment in bacterial biofilms, Microbiology 149 (2003) 1155–1163.
[20] G.S. Jiang, D. Peng, Weighted ENO schemes for hamilton-jacobi equations, SIAM J. Scient. Comput. 21 (2000) 2126–2143.
[21] S. Kathariou, *Listeria monocytogenes* virulence and pathogenicity, a food safety perspective, J. Food Protect. 65 (2002) 1811–1829.
[22] J. Kreft, C. Picioreanu, J. Wimpenny, M.C.M. Loosdrecht, Individual-based modelling of biofilms, Microbiology 147 (2001) 2897–2912.
[23] J. Kreft, J. Wimpenny, Effect of EPS on biofilm structure and function as revealed by an individual-based model of biofilm growth, water, Sci. Technol. J. 43 (2001) 135–141.
[24] R.J. LeVeque, Finite Difference Methods for Ordinary and Partial Differential Equations: Steady-State and Time-Dependent Problems, SIAM, 2007.
[25] P.D. Marsh, Dental plaque as a biofilm and a microbial community - implications for health and disease, BMC Oral Health 6 (2006).
[26] E.J. Marsh, B.L. Luo, H.A. Wang, three-tiered approach to differentiate *Listeria monocytogenes* biofilm-forming abilities, FEMS Microbiol. Lett. 228 (2003) 203–210.
[27] M.K. Miettinen, K.J. Björkroth, H.J. Korkeala, Characterization of *Listeria monocytogenes*from an ice cream plant by serotyping and pulsed-field gel electrophoresis, Int. J. Food Microbiol. 46 (1999) 187–192.
[28] T. Møretrø, S. Langsrud, *Listeria monocytogenes*: biofilm formation and persistence in food-processing environments, Biofilms 1 (2004) 107–121.
[29] M. Mosquera-Fernández, P. Rodrí-guez López, M.L. Cabo, E. Balsa-Canto, Numerical spatio-temporal characterization of *Listeria monocytogenes* biofilms, Int. J. Food Microbiol. 182 (2014) 26–36.
[30] M. Mosquera-Fernández, P. Sanchez-Vizuete, R. Briandet, M.L. Cabo, E. Balsa-Canto, Quantitative image analysis to characterize the dynamics of*Listeria monocytogenes* biofilms, Int. J. Food Microbiol. 236 (2016) 130–137.
[31] L.N. Mueller, J.F.C. de Brouwer, J.S. Almeida, L.J. Stal, J.B. Xavier, Analysis of a marine phototrophic biofilm by confocal laser scanning microscopy using the new image quantification software PHLIP, BMC Ecol. 6 (1) (2006).
[32] R.D. Noguera, G. Pizarro, D.A. Stahl, B.E. Rittmann, Simulation of multispecies biofilm development in three dimensions, Water Sci. Technol. 39 (1999) 123–130.
[33] S. Osher, J.A. Sethian, Fronts propagating with curvature-dependent speed: algorithms based on hamilton-jacobii formulations, J. Comput. Phys. 79 (1988) 12–49.
[34] C. Picioreanu, J. Kreft, M.C.M. van Loosdrecht, Particle-based multidimensional multispecies biofilm model, Appl. Environ. Microbiol. 70 (2004) 3024–3040.
[35] T. Pilchová, M. Hernould, H. Prévost, K. Demnerová, J. Pazlarová, O. Tresse, Influence of food processing environments on structure initiation of static biofilm of *Listeria monocytogenes*, Food Control 35 (2014) 366–372.
[36] A. Quarteroni, R. Sacco, F. Saleri, Numerical Mathematics, Springer-Verlag, New York, 2000.
[37] A. Rieu, R. Briandet, O. Habimana, D. Garmyn, J. Guzzo, P. Piveteau, *Listeria monocytogenes* EGD-e biofilms: no mushrooms but a network of knitted chains, Appl. Environ. Microbiol. 74 (2008) 4491–4497.
[38] P. Rodrí-guez López, P. Saá-Ibusquiza, M. Mosquera-Fernández, M. López-Cabo, *Listeria monocytogenes*-carrying consortia in food industry. composition, subtyping and numerical characterisation of mono-species biofilm dynamics on stainless steel, Int. J. Food Microbiol. 206 (2015) 84–95.
[39] J.A. Sethian, Level Set Methods and Fast Marching Methods, 2nd edition, Cambridge University Press, 1999.
[40] J.A. Sethian, Fast marching methods, SIAM Rev. 41 (1999) 199–235.
[41] S. Silva, P. Teixeira, R. Oliveira, J. Azeredo, Adhesion to and viability of *Listeria monocytogenes* on food contact surfaces, J. Food Protect. 71 (2008) 1379–1385.
[42] P. Stoodley, J.D. Boyle, D. DeBeer, H.M. Lappin-Scott, Evolving perspectives of biofilm structures, Biofouling 14 (1999) 75–90.
[43] B. Swaminathan, P. Gerner-Smidt, The epidemiology of human listeriosis, Microbes Infect. 9 (2007) 1236–1243.
[44] I.L. Tack, F. Logist, E. Noriega-Fernández, J.F.V. Impe, An individual-based modeling approach to simulate the effects of cellular nutrient competition on *Escherichia coli* k-12 MG1655 colony behavior and interactions in aerobic structured food systems, Food Microbiol. 45 (2015). Pt B:179-88
[45] N. Vyas, R.L. Sammons, O. Addison, H. Dehghani, A.D. Walmsley, A quantitative method to measure biofilm removal efficiency from complex biomaterial surfaces using SEM and image analysis, Sci. Rep. 6 (2016) 32694.
[46] O. Wanner, H.J. Eberl, E. Morgenroth, D.R. Noguera, C. Picioreanu, B.E. Rittmann, M.C.M. van Loosdrecht, Mathematical Modelling of Biofilms, IWA Task Group on Biofilm Modelling, 2006 Technical report.
[47] O. Wanner, W.G. O, A multispecies biofilm model, Biotechnol. Bioeng. 28 (1986) 314–328.
[48] P.A. Widerer, W.G. Characklis, Structure and function of biofilms, in: P.A. Widerer, W.G. Characklis (Eds.), Structure and Function of Biofilms, John Wiley & Sons, 1989, pp. 5–17.
[49] S.A. Wilks, H.T. Michels, C.W. Keevil, Survival of *Listeria monocytogenes* scott a on metal surfaces: Implications for cross-contamination, Int. J. Food Microbiol. 111 (2006) 93–98.
[50] J. Xavier, C. Picioreanu, M.C.M. van Loosdrecht, A modelling study of the activity and structure of biofilms in biological reactors, Biofilms 1 (2004) 377–391.
[51] J. Xavier, C. Picioreanu, M.C.M. van Loosdrecht, A framework for multidimensional modelling of activity and structure of multispecies biofilms, Environ. Microbiol. 7 (2005) 1085–1103.
[52] M. Zaborowska, J. Tillander, R. Branemark, L. Hagberg, P. Thomsen, M. Trobos, Biofilm formation and antimicrobial susceptibility of staphylococci and enterococci from osteomyelitis associated with percutaneous orthopaedicimplants, J. Biomed. Mater. Res. Part B 105B (2017) 2630–2640.